Tectonophysics 671 (2016) 95–109

Contents lists available at ScienceDirect

Tectonophysics

journal homepage: www.elsevier.com/locate/tecto

Contrasting amount of fluids along the megathrust ruptured by the 2010 Maule earthquake as revealed by a combined analysis of aftershocks and afterslip

Andres Tassara [a,*], Hugo Soto [a,b], Jonathan Bedford [b], Marcos Moreno [b], Juan Carlos Baez [c]

[a] Departmento de Ciencias de la Tierra, Facultad de Ciencias Químicas, Universidad de Concepcion, Victor Lamas 1290, Concepción, Chile
[b] Helmholtz-Zentrum, GeoForschungsZentrum–Potsdam, Telegrafenberg, Potsdam, Germany
[c] Centro Sismológico Nacional, Facultad de Ciencias Físicas y Matemáticas, Universidad de Chile, Blanco Encalada 2002, Santiago, Chile

ARTICLE INFO

Article history:
Received 18 March 2015
Received in revised form 7 January 2016
Accepted 8 January 2016
Available online 28 January 2016

Keywords:
Maule earthquake
Postseismic activity
b-value
Afterslip
Megathrust
Fluids

ABSTRACT

We present a novel approach combining time-variable computations of *b*-value and afterslip to study the postseismic activity following the Mw 8.8 Maule 2010 earthquake. We subdivided the first 392 days after the mainshock into overlapping windows, for which we compared maps of *b*-value (computed from NEIC seismicity) and afterslip (computed from continuous GPS stations). The correlation between both parameters is weak during the first 2 months when the aftershocks' magnitude of completeness decreases and the number of GPS stations increased. After this early stage, a correlation between both parameters emerges. We interpret this correlated spatiotemporal pattern combining factors proposed to control each parameter separately. This exercise suggests a segmentation of the Maule megathrust. The northern segment is characterized by an increase of afterslip and *b*-value during the early postseismic phase and then a simultaneous decrease of both parameters, which we interpret as the effect of an ingression of fluids into the megathrust and its subsequent consumption during fault healing. In contrast, the southern segment is characterized by a central region with minimum afterslip and low *b*-value surrounded by areas that experience mostly seismic afterslip as a consequence of large static stress loaded by the mainshock, suggesting a drier and stronger megathrust where healing was active earlier. Interpreted along with features of the pre- and coseismic phases, our results allow us to propose the existence of two contrasting types of seismic asperities: classical strong stick–slip patches that we link with dry regions of the megathrust, versus weak, wet and conditionally stable frictional patches that could have a range of seismogenic behaviors from creeping and/or locking during the interseismic period, largely contributing with coseismic slip, and concentrating afterslip at their borders. The application of our novel method to other great earthquakes could reveal whether this is a common or anomalous feature of megathrusts.

1. Introduction

In its simple original version (Lay and Kanamori, 1981), the asperity model imagines the seismogenic faults as formed by patches of high friction that are locked during the interseismic period and where coseismic ruptures can nucleate and propagate. Surrounding the asperities are regions of low friction that creep during the interseismic and postseismic phases therefore inhibiting the accumulation of elastic stress and acting as barriers for coseismic rupture propagation. Comparisons between interseismic locking patterns, coseismic slip, postseismic afterslip and aftershock distributions for great megathrust earthquakes that struck central Chile (Maule) in 2010 (Bedford et al., 2013; Lin et al., 2013; Agurto et al., 2012; Lange et al., 2014) and Japan (Tohoku-Oki) in 2011 (Johnson et al., 2012; Fukuda et al., 2013; Ozawa et al., 2012; Noda and Lapusta, 2013) are challenging this simple view. For the case of the Mw 8.8 Maule 2010 earthquake, analysis of aftershock seismicity (Lange et al., 2012; Rietbrock et al., 2012; Agurto et al., 2012) and afterslip derived from geodetic data (Bedford et al., 2013; Lin et al., 2013; Vigny et al., 2011) showed that a large percentage of aftershocks and afterslips were located in regions that experienced large coseismic slip (with some ambiguity derived from difference in available co- and postseismic slip models). This fact, added to the coincidence in some areas of moderate-to-high preseismic locking degree (Moreno et al., 2010; Moreno et al., 2012), large coseismic slip, large afterslip and dense small-magnitude seismicity, suggest that the model of time-persistent asperities and barriers interacting via static stress changes is, to some extent, incorrect.

In this manuscript, we study the first 392 days of postseismic activity following the Maule earthquake in an attempt to unveil the main physical processes taking place on the ruptured megathrust after such a large earthquake, and derive implications for the asperity model. We present

* Corresponding author.
E-mail address: andrestassara@udec.cl (A. Tassara).

http://dx.doi.org/10.1016/j.tecto.2016.01.009
0040-1951/

results of a novel method based on a combined spatiotemporal analysis of a previously published time-dependent afterslip model (Bedford et al., 2013) and aftershock seismicity. We investigate aftershocks by means of the frequency–magnitude relationship as parameterized by the *b*-value, which is the slope on the Gutenberg and Richter (1944) earthquake-size distribution. A robust body of knowledge has emerged during the past decade about the physical mechanisms controlling the *b*-value (see reviews by Wiemer and Wyss, 2002; Marzocchi and Sandri, 2003; El-Isa and Eaton, 2014). An important observation is that low/high *b*-values are characteristic of tectonic settings dominated by reverse/normal faulting, with strike-slip faulting showing intermediate *b*-values. Due to the large stress necessary to activate a reverse fault compared to a normal fault, this observation has led to the use of the *b*-value as a stress meter that points to low/high stress at faults showing high/low *b*-values (Schorlemmer et al., 2005; Scholz, 2015). In addition, a number of studies at different scales have shown that high *b*-values are observed in settings characterized by the pervasive circulation of fluids into rock fractures, suggesting that high pore pressures will reduce effective stress to generate a large number of small events with respect to greater events (e.g. Tilmann et al., 2008; Bachmann et al., 2012; Goertz-Allmann and Wiemer, 2012; Van Stiphout et al., 2009; Gischig and Wiemer, 2013). We computed maps of *b*-value for a number of time windows covering the period of analysis and extracted maps of cumulative afterslip for each of these windows. We compared both independent results in space and time, finding that they follow coherently distinctive temporal patterns but with remarkable differences in space. These differences were then interpreted into a conceptual framework, which unifies the relevant physical mechanisms that have been independently proposed to explain temporal changes of *b*-value and afterslip. This interpretation allows us to distinguish between regions where the postseismic activity is likely a consequence of fluid-assisted processes from other regions that are more likely dominated by static stress changes on a mostly dry megathrust, helping to resolve the ambiguity that commonly affects the interpretation of time-variable afterslip.

2. Seismotectonic setting of the Maule earthquake

The 2010 Mw 8.8 Maule earthquake ruptured the interplate boundary fault between the Nazca and South American plates along a segment of ca. 550 km long (34°S to 38.5°S, see Fig. 1). Its hypocenter was located near the center of the ruptured area (36.2°S) and the earthquake propagated bilaterally along the seismogenic zone. This earthquake closed a seismic gap of 175 years that was opened by the great 1835 Concepción earthquake (e.g. Melnick et al., 2012b).

The area affected by the 1835 event was surveyed by Sir Charles Darwin (Darwin, 1851) who described similar surface deformation pattern and tsunami effects as those reported for the 2010 Maule

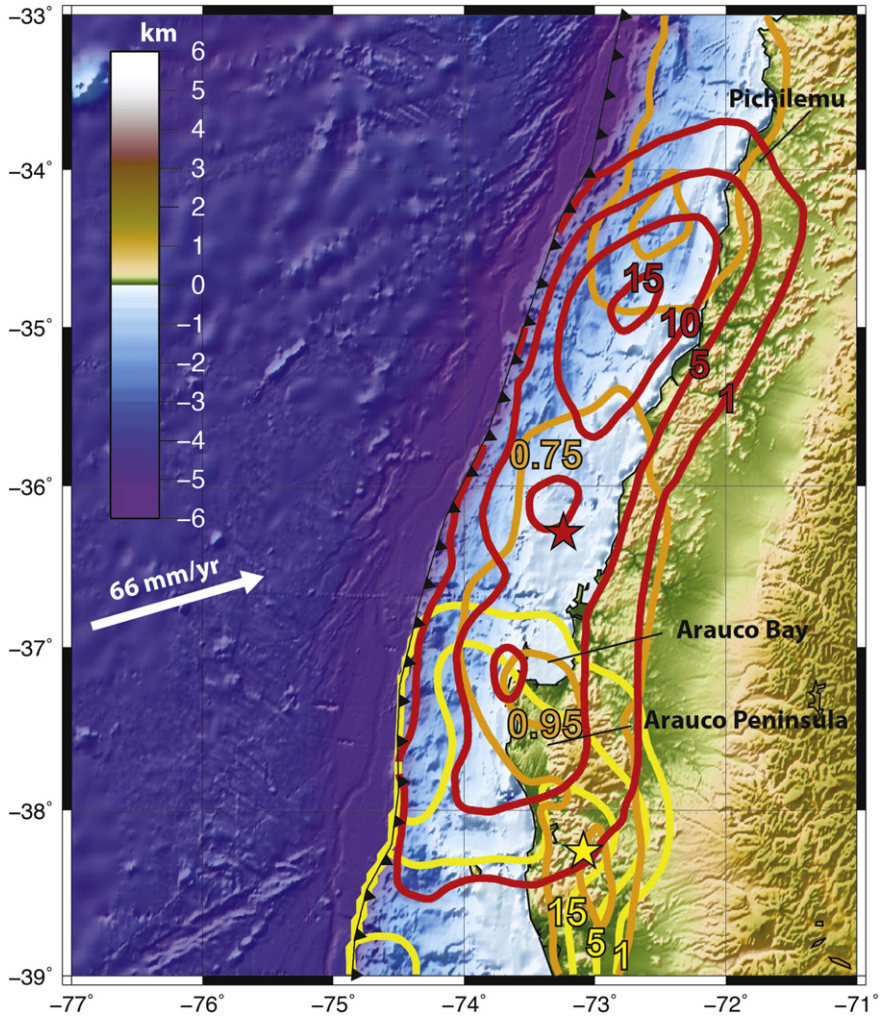

Fig. 1. Seismo-tectonic setting of the 2010 Maule earthquake at the Central Chile margin. Color map is topography/bathymetry (km) of the area. White arrow is the plate convergence vector (Kendrick et al., 2003). Yellow start is the epicenter of the 1960 Mw 9.5 Valdivia earthquake and yellow lines are contours in meters of coseismic slip for this earthquake (Moreno et al., 2009). Orange lines are contours of preseismic geodetic locking degree at the megathrust with respect to convergence velocity (Moreno et al., 2010). Red lines are contours in meters of coseismic slip for the 2010 Mw 8.8 Maule earthquake (Moreno et al., 2012). Red star is the epicenter of this earthquake as reported by the Chilean Seismological Survey.

event (Farías et al., 2010; Vargas et al., 2011; Fritz et al., 2011; Melnick et al., 2012a, 2012b). Seismic and geodetic data recorded during the earthquake have been inverted into a number of coseismic slip models (e.g. Lay et al., 2010; Delouis et al., 2010; Vigny et al., 2011; Lorito et al., 2011; Moreno et al., 2012; Tong et al., 2010; Bedford et al., 2013) that consistently shows one main slip patch (15–20 m) in the northern third of the ruptured area and other patches of large slip (>10 m) near the epicentral region and below the tip of the Arauco Peninsula (37.5°S). The Arauco region also experienced large coseismic slip (5–15 m) during the giant Mw 9.5 Valdivia 1960 earthquake (Moreno et al., 2009).

Inversion of surface displacement rates from GPS data into preseismic interplate locking for the decade before the Maule earthquake suggests that the megathrust was strongly locked (Ruegg et al., 2009) and that the spatial distribution of locking was rather heterogeneous (Moreno et al., 2010; Métois et al., 2012). The locking distribution shown by Moreno et al. (2010) exhibits a remarkable correlation with the pattern of coseismic slip mostly for the southern domain of the ruptured area below the Arauco Peninsula, although the larger slip patch in the north lays at the transition between a highly locked zone and a less locked region.

3. Data and methods

3.1. Analysis of aftershock seismicity

We concentrated on the first 392 days following the Maule mainshock. We selected aftershock seismicity contained in the USGS NEIC-PDE catalog into an area defined by coordinates 33°–40°S and 71°–75°W and magnitude larger than 4. This threshold was established because events with lower magnitude are very scarce in the NEIC-PDE catalog for this region, its location is arguable badly resolved and, as discussed later on, the magnitude of completeness of the catalog is well above this value. The resulting total number of events is 1884 quakes. The NEIC-PDE catalog for central Chile is mostly based on data recorded at teleseismic distance and therefore it is unable to detect small-to-moderate magnitude events. In addition, most of the epicenters of these events were located offshore and uncertainties on their location can be rather large (10–20 km) compared with what could be recorded by submarine OBS seismic networks as has been observed here (Lieser et al., 2014) and elsewhere (e.g. Geissler et al., 2010). However, the network configuration (number and position of seismic stations) does not change through time, meaning that for moderate-to-large magnitudes, the quality of the catalog remains homogeneous during the time frame analyzed here. This can be proved by analyzing the aftershock decay rate through time (Fig. 2). The number of earthquakes per day (N) for a given number of days after the mainshock (t) can be well fitted by the Omori law (Omori, 1894) $logN = (\frac{k}{c-t})^p$ if $k = 242.8$, $c = 0.26$ and $p = 0.96$. These numbers are typical for aftershock sequences following large earthquakes (Utsu et al., 1995; Wiemer and Katsumata, 1999), indicating that the aftershock catalog is complete for the magnitude range considered here and supporting its use to analyze the spatial–temporal behavior of aftershock seismicity after the Maule earthquake.

For different subsets of the seismicity catalog, we computed maps of the b-value that parameterizes the frequency–magnitude relationship given by the Gutenberg–Richter Law (GRL; Gutenberg and Richter, 1944). The GRL can be written as $logN = a - bM$ and it accounts for the number of earthquakes N with magnitude equal or larger than M for a group of events that occur in a given volume and time. The parameter a is the seismicity rate and the b-value is the slope of the linear trend defined by log$N$ versus M. We developed our own implementation of the widely used maximum likelihood method (Aki, 1965; Hamilton, 1967), by which the b-value can be estimated as $b = \frac{1}{\ln(10)*(M_{mean}-M_c)}$, with M_{mean} the average magnitude of the sampled events and Mc the magnitude of completeness above which earthquakes are reliably recorded by the seismic network. The uncertainty in the estimation of b-value is defined by $\Delta b = \frac{b}{\sqrt{N}}$, with N the number of events with magnitude equal or larger than Mc in the sample.

We first produced diagrams of the frequency–magnitude distribution (FMDs diagrams of Fig. 3) for subsets of the seismicity catalog that consider different latitude bands and time windows. This exercise was aimed at giving a first impression about the spatial and temporal variations of b-value and to analyze the ability of our method for retrieving relevant information from the NEIC catalog. Considering typical errors in the location of earthquake epicenter in the NEIC catalog (5–10 km) and the density of aftershock seismicity following the Maule earthquake, we then defined a regular grid of 0.1 × 0.1 degrees covering the studied region. For different subsets of the catalog, we computed maps of the b-value considering only those grid nodes where at least $Nmin$ earthquakes exist with magnitude equal or larger than Mc inside a cylinder of radius R. In order to ensure the comparability of results obtained from different sub-catalogs, we use a constant

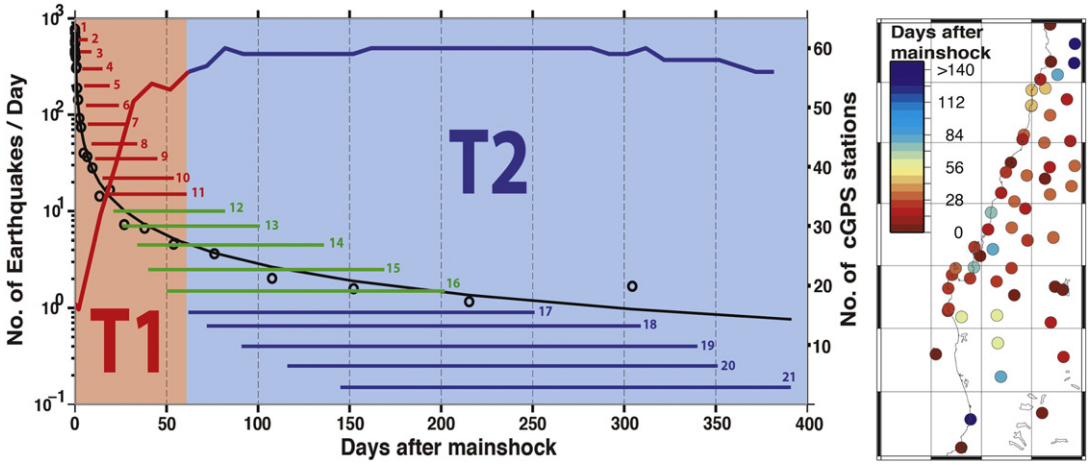

Fig. 2. Time evolution of aftershock seismicity and GPS stations over the region affected by the 2010 Maule earthquake. (Left) Circles and black line represent the daily number of earthquakes (left Y-axis) as fitted by Omori's law (see text). Red and blue lines show the number of cGPS stations displayed in the field through time (right Y-axis). Horizontal lines with numbers show time windows considered for extracting seismicity used for the computation of b-value maps of Figs. 4 and 5. The time interval T1 in red (time windows 1 to 11) is characterized by an increasing number of cGPS stations through time until a number of 56 stations is finally achieved 60 days after the mainshock, whereas for the time interval T2 in blue (time windows 17 to 21) the number of cGPS stations remains relatively stable. The transitional time interval TT in green (time window 12 to 16) overlaps T1 and T2. (Right) Map showing the spatial distribution of cGPS stations color-coded by the number of days after the mainshock when they were installed in the field.

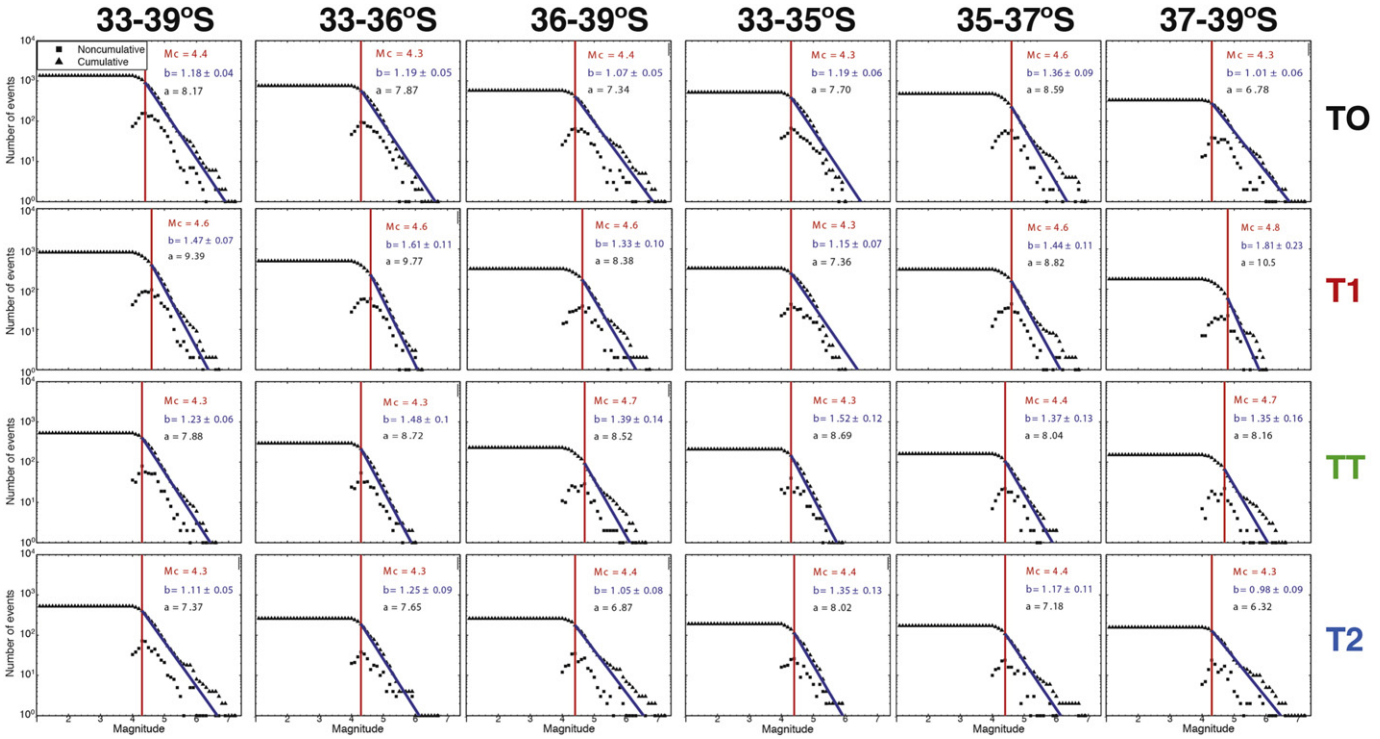

Fig. 3. Diagrams of the frequency–magnitude distribution (FMD) computed for given samples of the seismicity catalog. We considered the entire time period (TO) and divided the catalog in time following time windows T1, TT and T2 as defined in Fig. 2. For each FMD, we show the cumulative and non-cumulative number of earthquakes for a given magnitude range and the estimated value of *Mc*, *b*-value and *a*-value.

value of $Mc = 4.4$ for all our computations, which is the magnitude of completeness characterizing the entire catalog (Fig. 3). Section S1 of the Supplementary Material contains maps demonstrating that values of *Mc* computed as a function of the local sample of events do not change significantly in space and time, thus supporting our choice of a constant *Mc* value. The results presented below were obtained using $R = 100$ km (Fig. 4) or 150 km (Fig. 5) and $Nmin = 40$ events. We tested different values of these parameters (see Supplementary Material, Section S2) finding that smaller values of *R* (that could allow a more precise localization) and larger values of *Nmin* (that could reduce the estimated uncertainty) degrade the spatial resolution because fewer grid nodes surpass the computation criteria. However, for regions of dense seismicity, *b*-value maps with different *R* and *Nmin* values show the same amplitude of resolved anomalies. We also computed *b*-value maps using seismicity recorded by a temporal local seismic network covering the area of the Maule earthquake (Lange et al., 2012; Rietbrock et al., 2012), which have many more earthquakes with a much lower *Mc* than the NEIC catalog but concentrated in a shorter time interval. We find (Supplementary Material, Section S3) that the spatial variation of *b*-value mapped by these different catalogs is rather similar although the actual value of *b* decreases with decreasing *Mc*. Based on these tests, we will put more attention during our analysis to the first-order spatial variations of *b*-value than in the specific retrieved values of this parameter.

3.2. Inversion of cGPS time-series into megathrust afterslip

At the time of the Maule earthquake, 17 continuous Global Positioning System (cGPS) stations were operating in Central Chile (Vigny et al., 2011; Moreno et al., 2012; Bedford et al., 2013). During the first two months after the earthquake, the number of cGPS stations steadily increased until reaching a number of 56 stations (Fig. 2). The dense cGPS network installed in this region, being located very close to the trench (<100 km), gives a unique opportunity for observing time-dependent deformation processes associated with the postseismic phase of a great megathrust earthquake. Bedford et al. (2013) describes the details of methods for computing daily solutions of station position from these cGPS data and the inversion of these solutions into afterslip distribution at the megathrust interface. The method used PCAIM (Kositsky and Avouac, 2010) to invert these into daily time series rather than single cumulative displacements. Therefore, the output is a time series of daily slips at each grid node on the megathrust, from which we can extract the cumulative slip distribution for a given number of days grouped in specific time windows. PCAIM is based on dislocations of an elastic half space and does not consider viscous relaxation processes of both plates, which has been recently showed to greatly contribute to the postseismic deformation (Hu and Wang, 2012; Sun et al., 2014). Therefore, the afterslip model of Bedford et al. (2013) could be overestimated to a certain magnitude, although this effect is difficult to estimate without a dedicated modeling, but it is likely to be of long wavelength and distributed in a broad area.

3.3. Implementation of spatiotemporal analysis

Considering that the resolution and quality of the afterslip model were increasing with time due to the growing cGPS network, we divided the 392-day period of postseismic activity studied here into two main time windows (Fig. 2); T1 between the mainshock (27/02/2010) and the day immediately before the cGPS network acquired a stable configuration with 56 stations (29/04/2010; 62 days in total), and T2 between this day (30/04/2010) and the end of the studied period (25/03/2011; 330 days in total). We also defined a transitional time window called TT (20/03/2010 to 17/09/2010; 182 days in total) in order to better appreciate the changes between the two main windows.

With the aim of capturing the detailed spatial evolution of postseismic behavior with large temporal resolution, we subdivided the whole time frame into smaller sub-windows (Fig. 2). The first sub-window accounts for the first two days after the mainshock and contains 530 events. The other sub-windows were defined by considering a constant number of events (*Ne*) and an overlap of 85% of events between

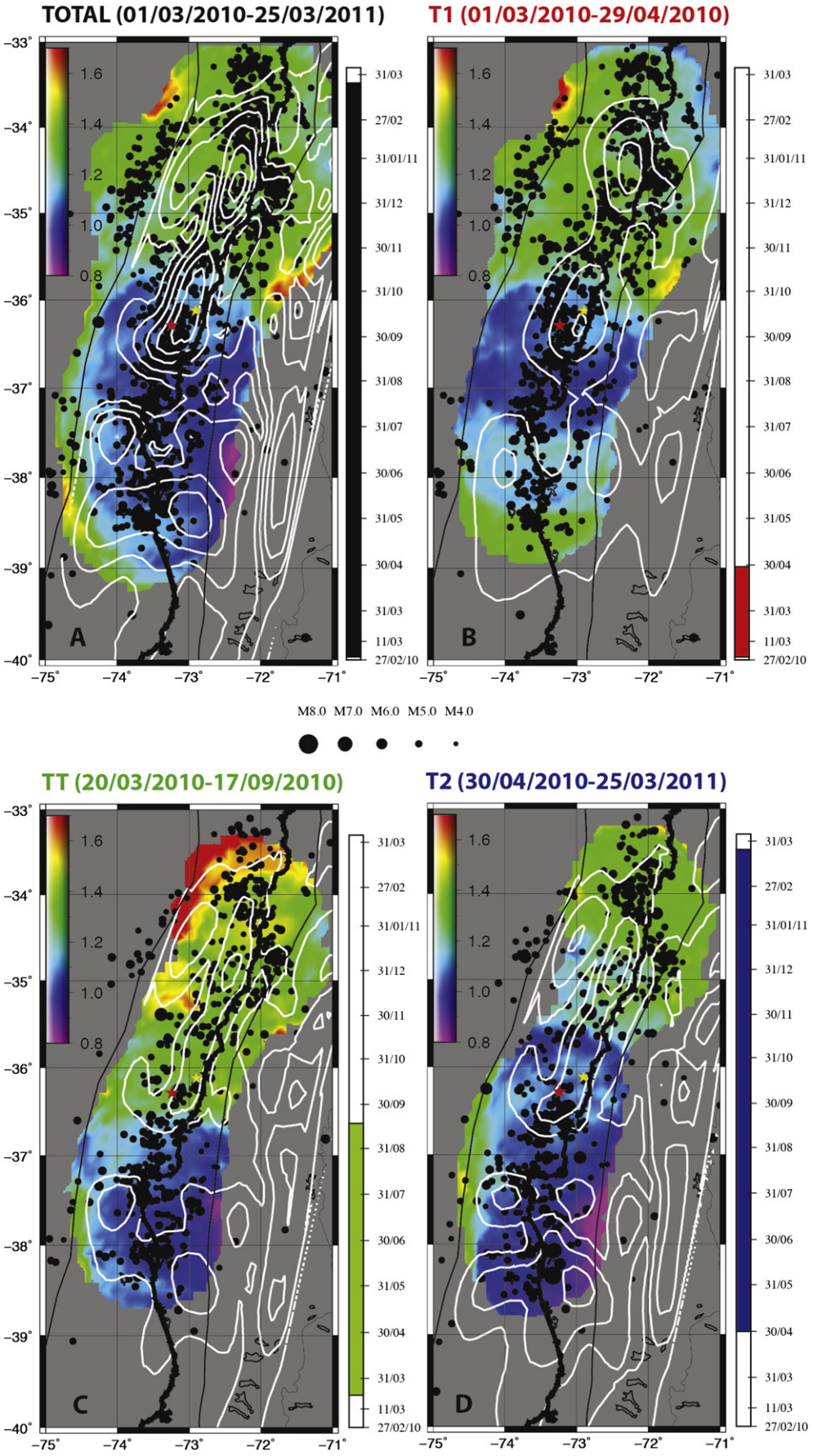

Fig. 4. Maps of *b*-value (color coding) and contours of afterslip every 0.3 m (in white). Black points are aftershock scaled by magnitude (see legend at the right). Time windows from left to right are TO, T1, TT and T2. Bars to the right of each map show the specific time lapse considered in each map.

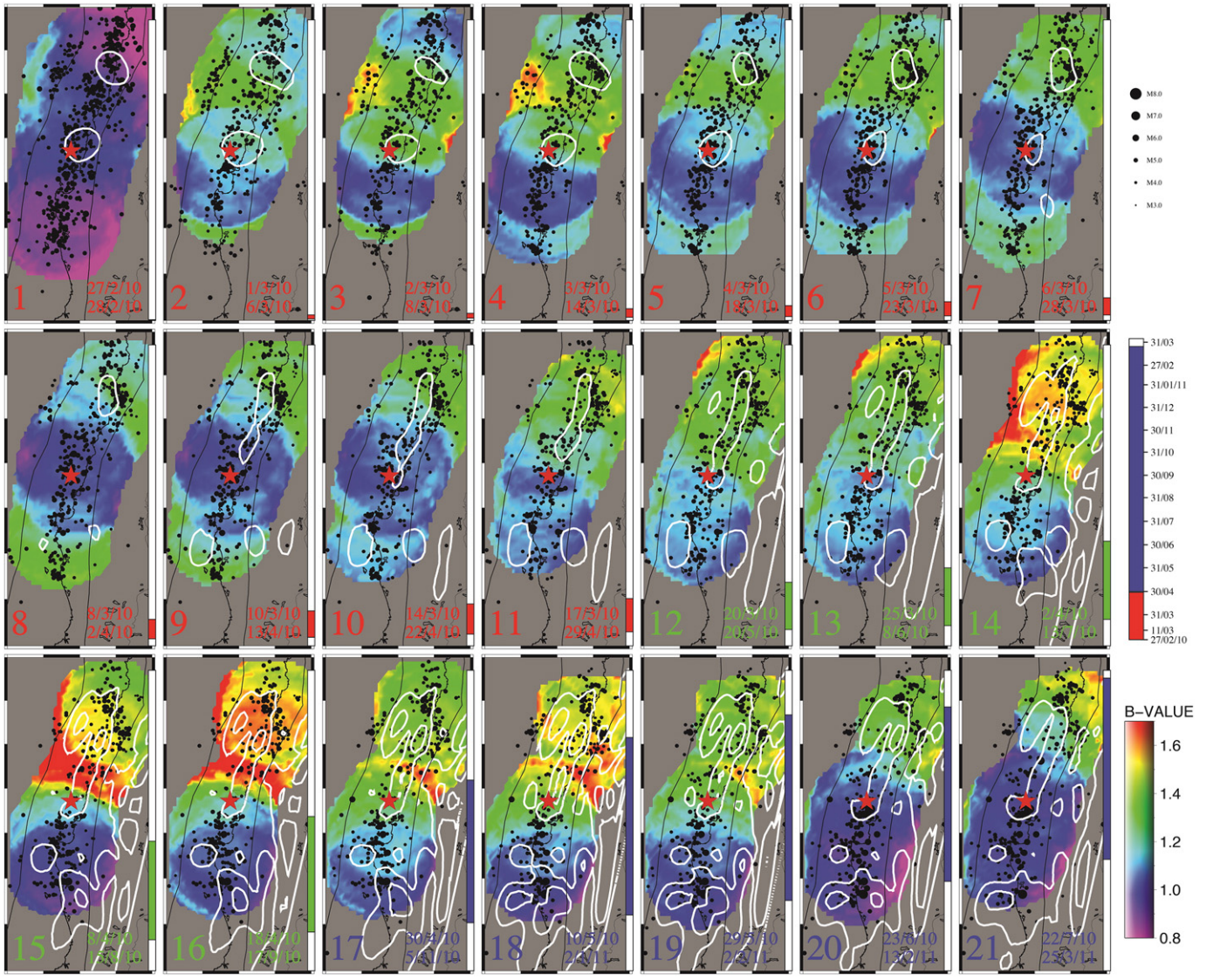

Fig. 5. Spatiotemporal evolution of *b*-value and afterslip. Each map shows the spatial distribution of *b*-value (colored with the color palette shown in the lower right corner) as computed from seismicity contained in each of the 21 time windows defined in Fig. 2. The column at the right-hand of each map represents the temporal extension of each window as referred to the column labeled Time in the lower right corner. Maps 1 to 11 during time T1 have a red bar, maps 17 to 21 during time T2 have a blue bar and maps 12 to 16 at the transition between them has a green bar. Afterslip cumulated during the same time window for each map is shown as white lines (contours every 0.3 m). Black circles are epicenters of earthquakes that occurred during each time window scaled by magnitude.

subsequent sub-windows. With $Ne = 345$ events, we got a total of 21 sub-windows and reached an optimal compromise between temporal resolution (increasing with lower *Ne*) and spatial coverage for each *b*-value map (increasing with higher *Ne*). The actual number of earthquakes contained in each sub-window oscillated between 291 and 365 (Supplementary Material, Section S4) because the unit of time of the afterslip model is one complete day and therefore we must adjust the number of days for each sub-window in order to contain a number of events as close to $Ne = 345$ as possible. Sub-window 2 started on the 1st of March 2010, avoiding the very early seismicity of the first two days. The first 11 sub-windows cover the main window T1, sub-windows 17 to 21 are for window T2 and sub-windows 12 to 16 are used to describe the transitional window TT. As the seismicity rate decays exponentially with time following the Omori–Utsu law (Fig. 2), sub-windows in the early postseismic phase cover a few days whereas those at the end of the analyzed period account for nearly 250 days. As the exponential decay of seismicity with time is remarkably similar to the decay of GPS westward displacement (e.g. Lange et al., 2014), considering a nearly constant number of earthquakes for sub-windows of increasing number of days with time also serves to normalize the total number of afterslips that cumulated in each sub-window. Therefore, this procedure ensures the comparability of results between different sub-windows.

The afterslip model does not include data for the 10th to 12th of March 2010 because Bedford et al. (2013) wanted to exclude from the computed megathrust afterslip the effect of two large crustal aftershocks (Mw 6.9 and 7) that occurred on the 11th of March in the Pichilemu area (34.5°S; Farías et al., 2011). To be consistent with this fact, we also excluded seismicity recorded during these days from our *b*-value analysis.

Considering vertical cylinders for the selection of seismicity used to compute the *b*-value at each grid node implies that we are taking quakes that occurred within the entire forearc volume. Well-located aftershocks following the Maule earthquake (Lange et al., 2012; Rietbrock et al., 2012) actually concentrate at or near the interplate boundary, but a percentage of events were located above (crustal faults) or below (intra-slab faults) the inferred megathrust surface. This could invalidate the comparison between the spatial distribution of *b*-value

and afterslip because the latter is supposed to be a process occurring exclusively at the megathrust. However, this is also an approximation because surface displacements observed by cGPS are also affected by the deformation of the entire forearc volume, which is mainly but not completely due to slip at the interplate fault (Bedford et al., 2013). In our analysis and discussion, we will assume that both parameters are manifestations of processes mainly occurring inside the megathrust but keeping in mind that crustal and intraslab faults also play a role as sources of both seismicity and deformation, mostly for some specific regions.

4. Results

4.1. First-order tendencies in the frequency–magnitude distribution

Diagrams for the frequency–magnitude distribution (FMDs) of earthquakes computed for different subsets of the seismicity catalog are shown in Fig. 3. We considered windows for the total time of this study TO and for times T1, TT and T2. We computed FMDs for the entire analyzed region (33–39°S) and for areas resulting after dividing the entire region into two (33–36°S, 36–39°S) and three (33–35°S, 35–37°S, 37–39°S) segments. First, we note that the logarithmic cumulative number of earthquakes generally follows a well-defined linear trend against magnitude, confirming the adequacy of the GRL and allowing the confident computation of *b*-value. Some FMDs however (e.g. TO and T1 at 35–37°S, TT at 37–39°S, T2 at 36–39°S) deviate from this linear trend at intermediate magnitudes. This deviation is commonly seen in published FMDs computed with the maximum likelihood method (e.g. Tormann et al., 2015; Legrand et al., 2012; Wiemer and Katsumata, 1999), which is not based on the direct fitting of the cumulative magnitude distribution but on the difference between the mean magnitude of the sample and the magnitude of completeness. Although a deviation from the GRL prediction for some time–space samples could incorporate uncertainty in the meaning of the *b*-value, we choose to apply our analysis in a systematic way attempting to extract first-order spatiotemporal variations of seismic activity that are mostly encapsulated in the computed mean magnitude of the sampled seismicity used by the maximum likelihood method for the calculation of the *b*-value.

With these considerations in mind, we note in Fig. 3 some tendencies in the space–time evolution of seismicity. First, we observe that the magnitude of completeness tends to decrease with time toward the value of the entire catalog ($Mc = 4.4$) that we choose for computing our maps of Figs. 4 and 5.

This would imply that for T1 along the entire region, and particularly for the southernmost area (37–39°S) where *Mc* during T1 is as high as 4.8, our choice of a constant $Mc = 4.4$ would underestimate the *b*-value. This fact, along with the uncertainty in the afterslip model during the first two months after the mainshock due to the increasing number of cGPS stations, implies that results for time window T1 must be interpreted with caution. Despite the variations of *Mc*, the *b*-value seems to decrease with time at the scale of the entire region and for most of the subregions. One important exception is the northernmost area (33–35°S) where *Mc* remains constant with time (4.3–4.4) but the *b*-value strongly increases between T1 (1.15) and TT (1.52) and then decreases to an intermediate value during T2 (1.35). Another first-order tendency is that the *b*-value tends to be higher in the north than in the south, a tendency that is more clearly seen after the first two months of T1, particularly during T2 where $Mc = 4.3$–4.4 for all the subregions.

With the aim of distinguishing these first-order tendencies in the space–time evolution of seismicity and to relate them with the evolution of afterslip, we computed maps of *b*-value for different time windows, as described below.

4.2. Qualitative description of large-scale space-temporal tendencies

Maps for the cumulative afterslip distribution and *b*-value computed for the entire period and for the three large time windows are shown in Fig. 4. In the Supplementary Material, we also show maps of the local *Mc* computed for each grid node (Fig. S1) and the estimated error of *b*-value (Fig. S3) to demonstrate that both are significantly uniform in space and time and that the error generally amounts to between 5% and 15% of the estimated *b*-value. Maps of *b*-value for the entire time period (Fig. 4a) and for window T1 (Fig. 4b) were computed excluding the 530 events recorded the first 2 days after the mainshock. This is because the first two days of seismicity represents more than a quarter of the total number of events considered here and nearly a third of those which occurred during window T1, and therefore obscures the space–time evolution of *b*-value at the scale of weeks to months that is of interest here for comparison with the afterslip.

The afterslip distribution accumulated during the entire 391 days period analyzed here (Fig. 4A) is dominated by distinctive patches of concentrated slip higher than 0.9 m. A large northernmost patch (34°–35°S) is formed by two NNE-elongated lobules, one near the trench axis with cumulated afterslip lower than 1.2 m and another directly westward from the coastline where afterslip reaches up to 1.8 m. This patch is separated by a region of reduced afterslip at 35.3°S from another coast-parallel large afterslip patch centered in the epicentral region of the mainshock. Notably, an area of near-zero afterslip is south of this patch around the Arauco Bay (37°S), which extends from the coast trenchward. To the south of this area, patches of relatively high afterslip (<1.2 m) surround the Arauco Peninsula. NNE-elongated patches of deep and large (>1.2 m) afterslip are located below the Andean cordillera to the east of the Arauco Peninsula and at the northern third of the studied region. The *b*-value map computed from seismicity recorded between 01/03/2010 and 25/03/2011 (Fig. 4A) shows a clear separation near 36°S. Northward from this latitude and coinciding with the large afterslip patch that dominates the northern third of the studied region, *b*-values are distinctively high (1.2–1.5) tending to decrease outside the northeast limit of this patch. South of 36°S *b*-values are lower than 1.1 almost everywhere with minimum values inside the seismogenic zone coinciding with regions of reduced afterslip.

We are interested in unveiling how the described distribution of cumulative afterslip and *b*-value evolves during the (approx.) first year of postseismic activity. We started computing combined maps of both parameters for time windows T1, TT and T2 as shown in Fig. 4B–D. Afterslip that accumulated during the first two months after the mainshock (window T1) shows almost all the features observed for the entire period but with nearly half of the total slip being cumulated during this early stage. For the approx. 11-month period that follows (window T2), these large afterslip patches grew to reach their final size, although some important changes also happened between T1 and T2: (a) the appearance of the western lobule of large afterslip (34.5°S, 73°W) and a slight southward migration of the coastal lobule (35°S, 72.5°S) at the northern third of the studied region, (b) connection between this latter lobule and the slip patch around the epicentral region (36°S, 73°S), (c) expansion of this patch trenchward, (d) reduction of afterslip to the east of the Arauco Bay and (e) intensification of the slip patch at the southern limit of the studied region (38.5°S, 73°S). All these changes are also seen in TT indicating that many of them took place during the first 4.5 months of T2. As for the entire period of time, maps of *b*-value were characterized by high values to the north of 36°S and low values southward of this latitude, although this general pattern changes with time. For T1, a nearly circular low-*b* region (*b*-value <1.1) covers an area between the epicentral region and the Arauco Bay (37°S, 73.5°W). Inside this low-*b* region, the large afterslip patch of the epicentral area is characterized by a slightly higher *b*-value (1.1–1.2). Toward the north and south of this low-*b* region, the *b*-value is higher than 1.2, reaching near 1.4 at the southernmost limit and northward from 35.5°S. The main change from T1 to T2 is

that the low-*b* region expands southward to cover the entire southern half of the studied region. However, window TT reveals that this expansion occurred in at least two steps: (1) an early (first 4.5 months of T2) southward migration of the low-*b* circular region from the epicentral area toward the Arauco Peninsula accompanied by an increase of afterslip in its southeastern limit, and a notable increase of *b*-values in the northern third of the region to values between 1.5 and 1.7 that occurs simultaneously with the activation of near-trench afterslip patches, and (2) a late (final 6.5 months of T2) northward expansion of the low-*b* region until reaching the northern end of the afterslip patch near the epicentral region and a decrease of *b*-value in the northern third of the studied region.

4.3. Quantifying the spatiotemporal correlation between afterslip and *b*-value

In order to get a detailed insight into the complex space-temporal evolution observed in maps of Fig. 4, we computed maps combining cumulative afterslip and *b*-value for each of the 21 sub-windows previously described (Fig. 5). These maps are complemented by maps of the error in the *b*-value (Fig S4) and estimations of the local *Mc* (Fig. S2). A detailed description of the space–time evolution of afterslip and *b*-value for these 21 sub-windows is not necessary here and is presented as part of the Supplementary Material (Section S5). Here, we only note that tendencies observed in large time windows (Fig. 4) are gradually acquired during sub-windows (Fig. 5) and that afterslip and *b*-value commonly change at a given region following a consistent spatial pattern pointing toward correlation between them. We think that this correlated space-temporal behavior of both parameters is indicative of a common process acting to regulate the temporal evolution of postseismic activity in the subduction system.

In an attempt to quantify these patterns, we performed two independent statistical analyses testing the degree of correlation between both parameters and the form that this correlation takes over the studied region. Here, we show the results of a linear regression analysis (Fig. 6). A computation of the Pearson's correlation factor that shows similar results is presented in the Supplementary Material (Section S6).

We considered sub-windows of time grouped in large time windows (TO, T1, TT and T2) and, at each grid node where at least 3 sub-windows contain estimates of cumulated afterslip (y) and *b*-value (x), we computed a linear regression line of the form $y = m^*x + c$ by minimizing the root mean squared (RMS) error. Maps of RMS error (Fig. 6 upper panel) help in quantifying the degree of linear correlation between both parameters (higher with lower RMS) and are complemented by maps showing the computed value for the slope m (Fig. 6, lower panel) of the line connecting them in time for each period.

Maps of RMS for the total period of time show that the degree of correlation between both parameters at the largest timescale is relatively low for the entire region, most clearly for areas surrounding the large northern coseismic slip patch and at the southwestern limit of the Arauco Peninsula (where RMS is as high as 20 cm). This is not surprising since our qualitative analysis already showed that for most of the studied region, the combined pattern of afterslip and *b*-value changed dramatically during the transitional window TT. Nevertheless, the map of the slope m for the entire period consistently shows a direct proportionality ($m > 0$) for most of the northern half of the studied region, with exceptions around the Pichilemu area, the coastal region at 35.3°S and to the northwest of the epicentral region (all areas of relatively strong correlation with low RMS error). Points characterized by positive

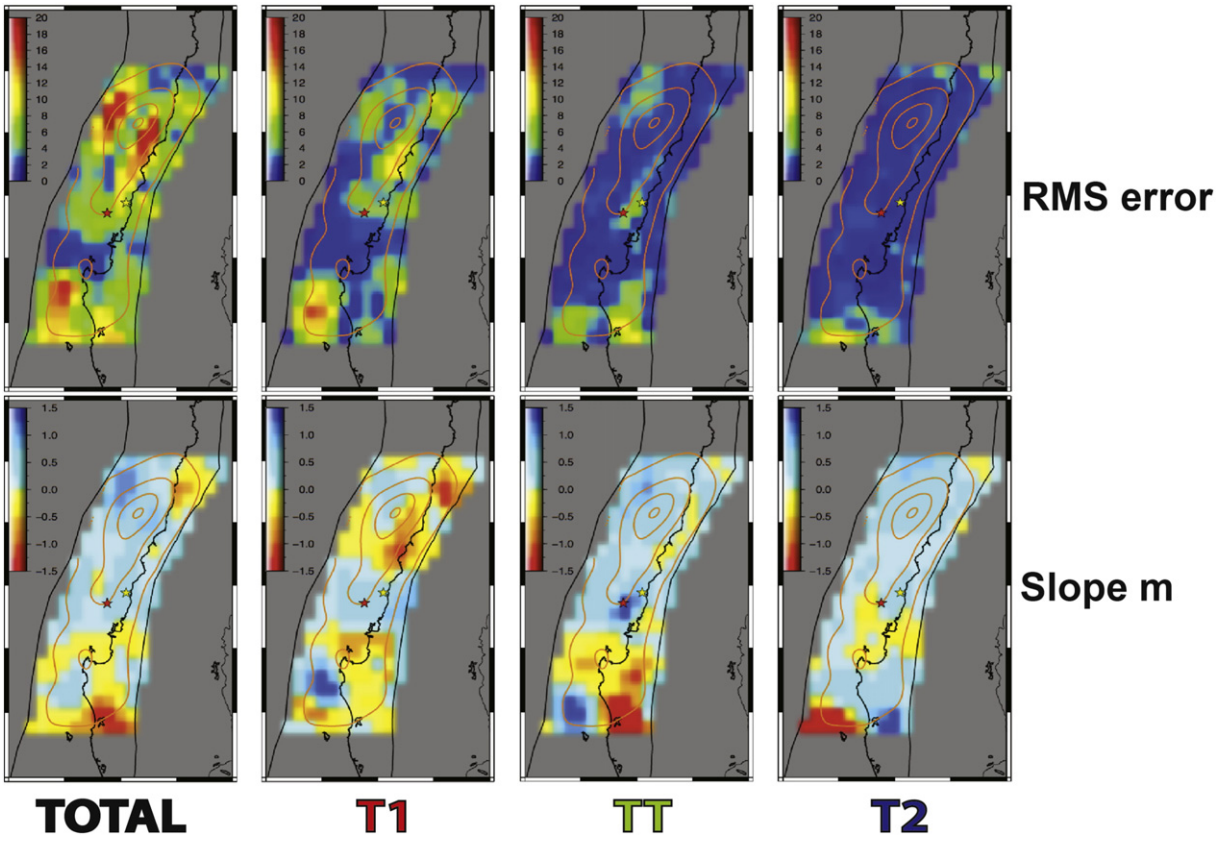

Fig. 6. Spatial correlation between *b*-value (b) and afterslip (as) for large time windows. For each colored point in these maps, the upper panel shows maps of the RMS error (in cm) of the adjusted linear trend defined by $as = m^*b + c$. Lower panel shows maps of the slope m characterizing this linear trend. Contours are for the coseismic slip every 4 m (Moreno et al., 2012).

values of the slope m show either an increase or a decrease of both parameters simultaneously. In contrast, a reverse proportionality ($m < 0$; increasing afterslip with decreasing b-value or vice versa) is mostly observed southward of 36.5°S, with the notable exception of a region to the southwest of Arauco Peninsula (where the correlation is weak).

Large differences in the degree of correlation and sign of proportionality can be appreciated by the inspection of maps for windows T1, TT and T2. For most of the studied region, the correlation shown in T1 is significantly weaker than for the other two windows. This could be a consequence of a combination of large uncertainties in the estimation of b-value because of differences between the constant Mc condition and the local Mc of the sample and the lower resolution of the afterslip model during T1 that could have an influence in the erroneous localization of afterslip patches and the estimation of its amplitude. However, the coverage of the cGPS network even for the first weeks after the mainshock (Fig. 2) was sufficiently good for capturing the main surface deformation pattern produced by megathrust afterslip, and therefore the relatively low degree of correlation during T1 could be a real fact. This could indicate that during this early phase of postseismic activity, afterslip and b-value fluctuate between a restricted range of values without a clear pattern between them through time. On the contrary, for TT and T2, the RMS error is almost everywhere lower than 4 cm, indicating that a strong linear correlation between both parameters was established after the early postseismic period (first month). It is striking that the form of the correlation (sign and actual values of slope m) during T1 is nearly the perfect opposite image to the one obtained for T2. Indeed, zones of reverse proportionality during T1 dominate in the northern half of the studied region and most of the Arauco region (Bay and Peninsula), but this tendency reverts completely during T2 showing for these zones strong direct proportionality. Notable exceptions to this reversing behavior are observed at the center of the largest coseismic slip patch and at the epicentral region, both showing positive values of m through time and strong correlation during T2, and at the Arauco Bay region which remains with negative, albeit low, values of m during the entire period.

The spatial pattern of correlation depicted for the transitional window TT helps identifying more concretely when the shift between T1 and T2 was produced. Interestingly, maps of m for TT and T1 are very similar only for the southern half of the studied region, whereas T2 and TT are almost identical for the northern half. This indicates that the shift from neutral-to-reverse proportionality (T1) toward direct proportionality (T2) was accomplished first (early 4.5 months of T2) in the northern half of the studied region and then (last 6.5 months of T2) below the central part of the Arauco Peninsula. At the northeast and southwest limits of the Peninsula, opposite changes (from direct to reverse proportionality) also occurred in the late period of T2. Another interesting feature revealed by maps of Fig. 6 is the temporal change in the slope of linear trends defined between afterslip and b-value. Positive and negative slopes during T1 are rather flat ($-0.5 < m < 0.5$) but they strongly steepen during TT, mostly in the southern half of the studied region. The reversal in the sign of correlation between TT and T2 at this southern region also occurs with steep gradients, most clearly at the southernmost limit of the studied area. To the north of 36°S, positive values of m remain almost unchanged between TT and T2.

5. Discussion and conclusion

Our results show that the number of afterslips cumulated at a given time window and the b-value characterizing the seismicity occurred during the same time remarkably change in space and time (Figs. 4 and 5). The spatial correlation pattern showed by Fig. 6 (mostly for time windows TT and T2) indicates that both parameters are likely coupled to common physical processes governing the postseismic evolution of the ruptured megathrust. We focus our discussion on unveiling the nature of these processes in order to compare factors controlling the postseismic phase of the Maule earthquake with those likely dominating its pre- and coseismic behavior. This exercise could help in evaluating the asperity model for frictional behavior of the megathrust and improving our understanding of the mechanisms that destroy and reconstitute friction during the seismic cycle.

5.1. Building a conceptual framework for common interpretation of afterslip and b-value

In order to give an adequate framework for discussing our results, we take advantage of our strategy based on analyzing two independent parameters (afterslip and b-value) that have been previously interpreted separately in terms of relevant processes. We summarize this interpretative base on the diagram of Fig. 7, which represents the quadrants of a generalized b-value vs. afterslip parameter space useful for analyzing the temporal evolution of both parameters at a given point of the megathrust.

Temporal variations of afterslip are commonly interpreted into the framework of a rate-dependent friction law (Dieterich, 1979; Ruina, 1983; Scholz, 1998), which approximates friction μ as

$$\mu = \mu_0 + (A-B)\ln\frac{V}{V_0}$$

Changes in friction with respect to its long-term static value μ_0 are caused by variations of the slip rate V with respect to the long-term tectonic loading rate V_0. The effect of slip transients is thus regulated by material properties of the fault parameterized by $(A - B)$. For regions on the fault where $(A - B) > 0$, friction will always increase after a rapid slip pulse (rate-strengthening regime) potentially arresting the propagation of coseismic rupture (a barrier). Empirical values of $(A - B)$ are dominantly controlled by temperature T (Scholz, 1998; Den Hartog and Spiers, 2013), with negative values for 150 °C–100 °C < T < 350 °C–400 °C. This temperature range coincidently defines the trench–normal extent of the seismogenic zone of subduction megathrusts (e.g. Oleskevich et al., 1999). Up- and down-dip of this zone, sliding of rate-strengthening regions would be possible as slow aseismic creep during the interseismic period and/or as postseismic afterslip for areas positively loaded by the static stress change caused by coseismic rupture (as parameterized by the Coulomb failure stress change ΔCFS). Inside the seismogenic zone where $(A - B) < 0$ the fault will experience a decrease on friction after a slip pulse (rate-weakening

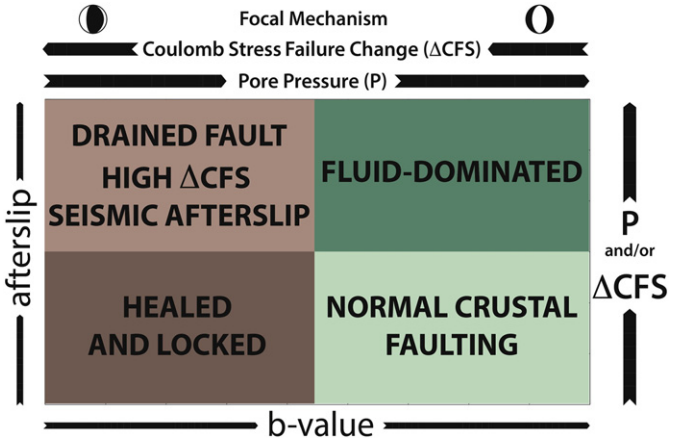

Fig. 7. Parameter space of b-value vs. afterslip exploring the relationship between both parameters in terms of relevant physical processes. An increase of afterslip at a given point can be associated either to an increase of Coulomb failure stress (ΔCFS) as loaded by the mainshock and/or neighboring patches of (possibly seismic) afterslip, or by an increase in pore fluid pressure (P). An increase of b-value is related to this later alternative and to a decrease in ΔCFS with a change in dominant focal mechanism. This combination offers the possibility for a more robust interpretation of time evolution of both parameters as summarized by the concepts expressed in each quadrant (see text for discussion).

regime). However, the actual behavior depends on the balance between the elastic stiffness kL of material surrounding the fault, the normal stress σ loading the fault and the pore pressure P inside the fault (Scholz, 1998; Perfettini and Avouac, 2004). If $(\sigma\text{-}P)$ is sufficiently large, then-$(A\text{-}B)(\sigma\text{-}P)>kL$ and an unstable stick–slip behavior is promoted; the fault is locked during the interseismic period, frictional instabilities develop in the form of earthquakes and afterslip is minimized because of the rapid healing of frictional contacts (an asperity). With relatively low normal stresses and/or high pore pressures, then -$(A\text{-}B)(\sigma\text{-}P)<kL$ and the fault is in a conditionally stable regime. Dynamic numerical modeling of the seismic cycle (e.g. Kaneko et al., 2010; Barbot et al., 2012; Noda and Lapusta, 2013) have demonstrated that this regime is able to produce a rich range of frictional behaviors, from creeping at slow rates under quasi-static loading to locking before an earthquake and efficient propagation of coseismic rupture if affected by the arrival of an earthquake propagation front at sufficiently large velocity, mostly if a mechanism of velocity-activated weakening is operating (Noda and Lapusta, 2013; Hirono et al., 2013).

Into this framework and summarizing conclusions of previous authors (Perfettini and Avouac, 2004; Perfettini et al., 2010; Lin et al., 2013; Hsu et al., 2006; Johnson et al., 2012; Fukuda et al., 2013), the amount of cumulated afterslip in a given amount of time should increase (from bottom to top in Fig. 7) with increasing ΔCFS, increasing pore pressure P, decreasing $(A - B)$ and decreasing kL. In our analysis, we mostly considered possible transient changes on static stress and pore pressure because the effect of changes on material parameters at the scale of months is difficult to constraint and arguably of minor relevance compared with those on ΔCFS and P.

The sole analysis of afterslip variations in space and time cannot be unambiguously used to distinguish between effects due to changing static stress, pore pressure or material properties (Bedford et al., 2013; Lin et al., 2013). Interpreting spatiotemporal variations of the b-value as an independent variable help us disentangle the potential role of possible controlling factors. A number of studies at the scale of laboratory experiments (Scholz, 1968; Goebel et al., 2013), hydrothermal reservoirs (Bachmann et al., 2012; Goertz-Allmann and Wiemer, 2012) and large-scale seismotectonic regions (Schorlemmer et al., 2005; Tilmann et al., 2008; Legrand et al., 2012; Tormann et al., 2015; Scholz, 2015) can be summarized by stating that b-value should increase (from left to right in Fig. 7) with decreasing ΔCFS, increasing pore pressure P and increasing relative number of intermediate-to-small magnitude earthquakes with dominantly normal focal mechanisms.

This analysis shows that changes on static stress (ΔCFS) have opposite effects on the amount of afterslip and b-value. This would imply a negative correlation in time between both parameters with changing ΔCFS, i.e. negative values of the slope m in Fig. 6. On the contrary, changes in pore pressure move both parameters in the same direction, implying positive values of m. Under constant material properties, this allows us to unveil the relative role of varying ΔCFS and P in controlling spatiotemporal variations of the postseismic activity.

By applying this conceptual framework to the analysis of our results, we will mostly focus on processes likely taking place at the megathrust. However, it is important to consider that the b-value is computed at each grid point from seismicity recorded inside a vertical cylinder centered at that point, so mapped b-values average seismicity that also occurred in the upper and lower plates, not only at their boundary. In this sense, if interplate and intraplate seismicity are both present and respond to fundamentally different processes, then it would be difficult to use the scheme in Fig. 7 to unveil the role of these processes. We will consider this point when interpreting our results, but we recall that previous studies using a dense local seismic network (Lange et al., 2012; Rietbrock et al., 2012) and a submarine OBS deployment (Lieser et al., 2014) located a great majority (>85%) of aftershocks at or near the interplate boundary, with significant upper plate seismicity concentrated in well-defined regions.

5.2. Application to postseismic activity after the Maule earthquake

In order to better appreciate the wide range of postseismic behavior that can be inferred from our results and to interpret them into the conceptual framework previously defined, Fig. 8 depicts the temporal evolution of b-value and cumulated afterslip at 10 selected points. Linear tendencies between both parameters for time windows T1, TT and T2 as shown in this figure were used to compute values of the slope m and RMS error in Fig. 6. We put more attention to points inside the region of superior spatial resolution of the afterslip model (as reported by Bedford et al., 2013). Fig. 8 shows that points located in different regions of the coseismically ruptured area experienced a consistently different temporal behavior in afterslip and b-value. This translates into the particular spatial pattern and temporal variability of the correlation between them, as observed in Fig. 6.

We first note that the lower-left quadrant of Fig. 7 corresponds to a dominantly stick–slip rate-weakening frictional regime loaded under high stress levels and characterized by dry fault conditions (low pore pressure). Points falling into this quadrant (like points H and I of Fig. 8) can be considered as forming part of already locked asperities. They are either patches mostly un-ruptured by the mainshock owing to their high static friction (point H and Arauco Bay area to the north of it) or regions ruptured by the coseismic propagation front but where healing has already reconstituted fault friction (point I). Almost all other points in Fig. 7 show a more (B, C, D, F, J) or less (E and G) clear pattern toward the lower-left quadrant during time T2, which makes the map of slope m for this time window dominated by positive values, mostly in the northern half of the ruptured area (Fig. 6). We think that this tendency is indicative of a process of ongoing healing, i.e. re-strengthening of the ruptured fault driven by the reconstitution of frictional contacts.

If the simultaneous movement of afterslip and b-value from the upper-right quadrant (which following our interpretation is dominated by high fluid pressure) toward the lower-left quadrant is actually related to fault healing, our analysis suggests that this process is mostly controlled by the reduction of pore pressure through time. This in turn could be due to the consumption of pore fluids either by crystallization of gauge minerals and/or pressure solution reactions at frictional contacts (Marone, 1998; Yasuhara et al., 2005), or to the escape of fluids from the fault interface through a fractured forearc toward the surface (Sibson, 2013; Koerner et al., 2004). In both cases, our results show that, for most of the studied region, the healing process (simultaneous reduction of afterslip and b-value) started between TT and T2, i.e. some months after the mainshock. This delay is consistent with expectations guided by laboratory experiments and the rate-and-state friction law (Marone, 1998; Nakatani and Scholz, 2006).

At the northern half of the ruptured segment (points B, C, D), healing during T2 did follow a peak in afterslip and b-value after a period (coinciding with TT) when they were gradually increasing. Being consistent with our previous argumentation, this movement from the center of the parameter space in T1 toward the upper-right quadrant of Fig. 7 during TT must be interpreted as a pulse of fluids invading pores of the fault at high pressure. The increase in b-value is thus likely due to the larger number of small-to-intermediate magnitude events triggered by the decrease in effective normal stress caused by higher pore pressure. Furthermore, the large negative static stress change (Lorito et al., 2011; Bedford et al., 2013) and rotation of the stress field produced by an almost complete stress drop on the ruptured fault (Hardebeck, 2012) could be also responsible for augmenting the quantity of relatively small earthquakes with dominantly normal focal mechanism. The return of the stress field to its pre-mainshock configuration some months after the Maule earthquake as suggested by the analysis of focal mechanisms (Hardebeck, 2012) also supports a delayed start of fault healing in this region.

If the percolation of fluids on the megathrust is important for interpreting the simultaneous increment of afterslip and b-value in

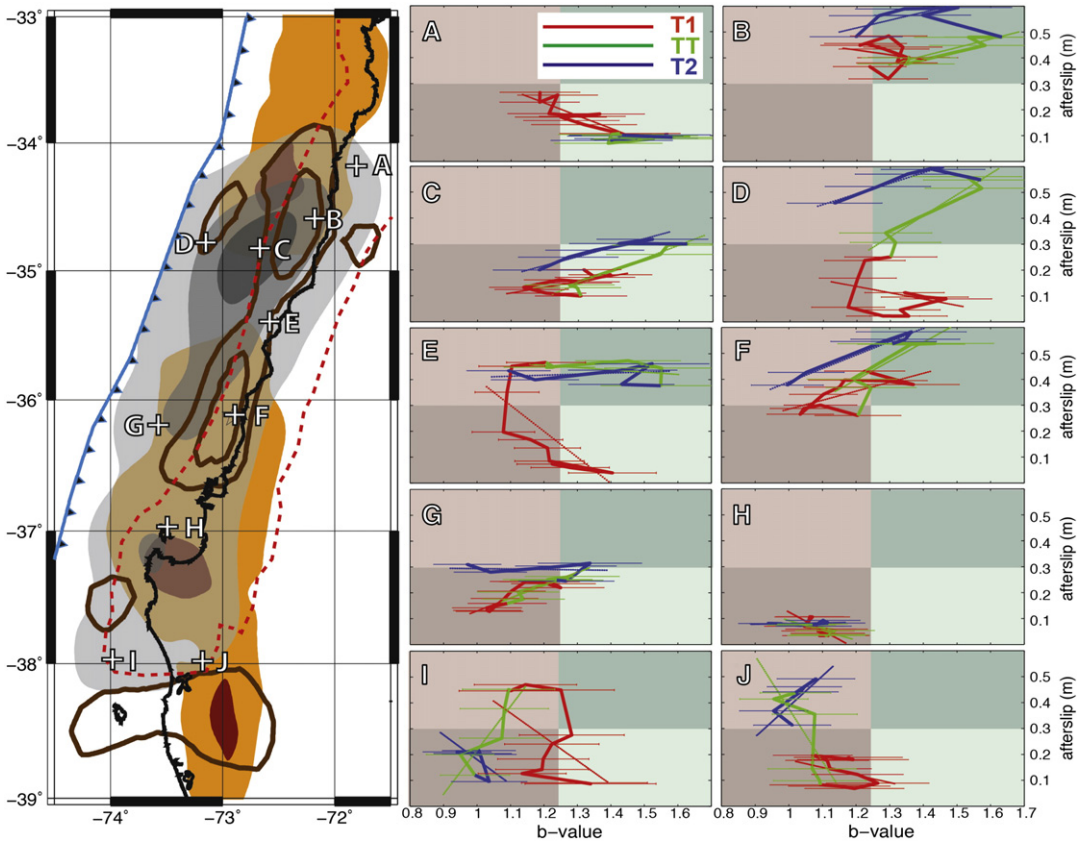

Fig. 8. Temporal evolution of *b*-value and afterslip for 10 selected points. Map at the left shows interseismic locking (orange-brownish areas at 75% and 95% convergence; Moreno et al., 2010), coseismic slip (gray areas with transparency for contours every 4 m; Moreno et al., 2012), total cumulative afterslip (brown contours for 0.9 and 1.5 m; Bedford et al., 2013), the region of superior spatial resolution of afterslip model (red dashed line; Bedford et al., 2013) and location of points depicted at panel A to J at the right of the figure. For each of them, lines are constructed connecting points extracted from maps of sub-windows 2 to 21 in Fig. 5 and colored for corresponding time windows T1 (red), TT (green) or T2 (blue). Error bars are available for *b*-value. Colors at the back of each panel refer to those of Fig. 7.

the northern region during TT, then a physical mechanism as to be advocated to explain this percolation. We think that the source of fluids should be the subducting slab below an impermeable seal formed by the locked megathrust before the mainshock. Such seals have been imaged seismically in other subduction zones (i.e. Audet et al., 2009; Calahorrano et al., 2008) as layers of augmented seismic velocities at the interplate fault above anomalously low velocity regions interpreted as fluid reservoirs into the oceanic crust and mantle. These seals are broken by the mainshock and fluids are able to escape permeating the fault and eventually invading the forearc crust (i.e. Koerner et al., 2004). Our results suggest that this process, if it actually occurred after the Maule earthquake, took place mostly in the northern half of the ruptured area (north of 36.5°S) and its effect on simultaneously increasing afterslip and *b*-value was apparent after the first couple of months of postseismic activity (entering period TT). This in turns suggests that the ingression of fluids into the megathrust could be localized in some point near the largest coseismic slip patch and that percolation to the rest of the fault is not instantaneous, suggesting a diffusion-like mechanism of fluids into a porous media.

The fluid-dominated process that characterizes the northern half of the ruptured area seems to be absent south of 36.5°S, as revealed by an inspection of maps for the slope *m* (Fig. 6) and points south of this latitude in Fig. 8. Negative values of *m* for most of the onshore region of the Arauco Peninsula during TT and the tendencies of points I and J into the parameter space, suggest that an increase of afterslip at constant or decreasing *b*-value is related to the relaxation of large static stresses loaded by the mainshock in conditions of relatively low pore pressure of the megathrust. A relatively dry megathrust fault for this same region has been proposed by Moreno et al. (2014) based on the correlation of large interseismic geodetic locking and relatively high Vp/Vs ratio as inferred from seismic tomography before the Maule earthquake. This interpretation is also consistent with the maximum coefficient of effective friction (which increases with decreasing pore pressure) computed by Cubas et al. (2013) from critical taper angles for the onshore Arauco Peninsula compared with the rest of the area ruptured by the Maule earthquake. Our interpretative diagram (Fig. 7) also indicates that under relatively dry conditions, the release of the static stress change does occur mainly as seismic afterslip, i.e. slip mostly produced by aftershocks. In this respect, negative values of the slope *m* in Fig. 6 for the Arauco region during TT are notably similar and perfectly consistent with large seismically released afterslip (Agurto et al., 2012), large cumulative seismic afterslip (Lange et al., 2014) and high aftershock seismic efficiency (Bedford et al., 2013) for the same region. The reversal of this tendency during T2 (Figs. 6 and 8) for most of the ruptured area south of 37°S suggests that static stresses left after the mainshock were already consumed (decreased) a year after the mainshock and the fault rapidly heals in this region later on.

5.3. Bending-related fracturing of the oceanic plate and fluid transport below the seismogenic zone

The reason why fluids seem to dominate in the northern half of the Maule segment compared with the persistently dry megathrust in the south could be the more pervasive fracturing of the incoming oceanic plate in the north, as can be observed in Fig. 1 and has been also suggested by Moscoso and Contreras-Reyes (2012). Oceanic plate fracturing is mostly a consequence of flexural bending as the plate approaches the trench axis (e.g. Ranero et al., 2003; Faccenda et al., 2009). The wavelength of flexural bending, and hence the potential for producing bending-related fractures, decreases southward along

the south-central Chile margin (Contreras-Reyes and Osses, 2010) as the Nazca plate becomes younger approaching the Chile Rise (at 46.5°S), reducing its elastic thickness and the capacity for resisting bending stresses. A pervasively fractured oceanic plate like the one subducting northward of 35.5°S is able to absorb large amounts of seawater that percolate its crust and upper mantle reducing seismic velocities, as seen in many seismic images of subduction zones (e.g. Ranero et al., 2003; Grevemeyer et al., 2007; Calahorrano et al., 2008). In the case of the Maule segment, Contreras-Reyes et al. (2007, 2008); Moscoso et al. (2011); Moreno et al. (2014); Hicks et al. (2012, 2014) show that seismic velocities of the bending slab in the northern half of the Maule segment are significantly lower than toward the south. Particularly, Hicks et al. (2014) show that Vp along the plate interface (as imaged by a 3D seismic tomography considering data after the 2010 earthquake) is much lower in the north (5.5 km/s) than in the south (>6.5 km/s) for a significantly larger Vp/Vs ratio in the north (1.9 versus 1.75), which translates to a very low Vs suggesting larger amount of fluids. This image is complemented by the gravity modeling of Maksymowicz et al. (2015) who showed a decreased crustal density above the northern portion of the rupture area, and low effective basal friction coefficient estimated by Cubas et al. (2013) based on a critical taper analysis of bathymetry and slab geometry. These observations suggest that it is not only the short-term postseismic behavior after the Maule earthquake that is likely dominated by fluids in the northern part ruptured area but also the long-term (millions of years) geological structure of the forearc, reinforcing the idea that the increased fracturing of the oceanic plate as created at the same timescale plays a relevant role.

Percolated fluids into the slab are stored into clay minerals and serpentinite (e.g. Ranero et al., 2003) and then released below the forearc as higher pressure and temperature favors dehydration reactions. These fluids are trapped below the megathrust if it is sealed, as suggested by detailed seismic images of some forearcs (e.g. Audet et al., 2009; Calahorrano et al., 2008), and could be eventually released into the megathrust when the seal is broken by the propagation of an earthquake rupture front. Our results suggest that this process actually took place in the northern half of the Maule rupture area.

5.4. Crustal normal faulting and fluid escape into the forearc

An outlaying point with respect to the rest of the study region is point A (Fig. 8) near the Pichilemu region. This point shows a rapid motion toward the right-lower quadrant of the parameter space during the first months after the mainshock (T1) with decreasing afterslip for increasing *b*-values that remains at the lower and upper limits (respectively) of the diagram for TT and T2. Our interpretation is that this region is largely affected by mostly crustal seismicity of small magnitude and normal focal mechanism related to the large (Mw 6.9–7) normal-faulted aftershocks that occurred here on the 11th of March (Farías et al., 2011; Ryder et al., 2012). High *b*-values are likely a consequence of large negative static stress changes after the mainshock (Hardebeck, 2012) and/or high pore pressure into these crustal faults reflecting the escape of fluids from the megathrust to the upper crust, as suggested by high Vp/Vs ratios (Farías et al., 2011). The activity of these faults could have drained large amounts of fluids from the megathrust, helping to reduce the pore pressure at the interplate fault and to initiate its healing process, at least at the northernmost extend of the ruptured region.

5.5. Comparison with pre- and coseismic behavior

Our results and their interpretation suggest that the postseismic activity of the Maule megathrust and its variation along-strike are probably controlled by a variable amount of fluids as a likely consequence of long-term difference in the structure of the subducting plate. Particularly, the inferred presence of fluids in the northern half of the rupture area implies high pore pressure that could promote a conditionally stable frictional regimen, whereas lower pore pressure around the Arauco Peninsula in the south favors a stick–slip behavior. Into this framework, we explore the possibility that the pre- and coseismic behavior before and during the Maule earthquake could also reflect this supposed control of fluids on frictional regimen. In order to perform this exercise, we use the preseismic locking model of Moreno et al. (2010) and the coseismic slip model of Moreno et al. (2012), because they were constructed under the same geometry and parameterization as the afterslip model of Bedford et al. (2013).

First, we note that the epicentral region, the postseismic behavior of which is characterized by point F in Fig. 8, shows signs of being dominated by fluids perhaps from the very early stage after the mainshock. This is similar to what can be inferred from points inside (C) and around (B, D, E) the main coseismic slip patch in the northern third of the ruptured segment. Following our interpretation, the epicentral point should have a conditionally stable frictional behavior owing to its high pore pressure, which is considered unfavorable for the nucleation of seismic rupture (e.g. Scholz, 1998). However, seismic images (Hicks et al., 2012, 2014) and gravity anomalies (Tassara, 2010; Hicks et al., 2012) suggest that the epicentral region coincides with a prominent high-velocity/high-density body at the megathrust probably related to a large subducted seamount. This bathymetric and compositional anomaly (with respect to the more common small seamounts that can be seen in Fig. 1) could create an anomalously high normal stress, as proposed elsewhere (Contreras-Reyes and Carrizo, 2011; Sparkes et al., 2010), which could shift the frictional regimen into the stick–slip rate-weakening field for which earthquake nucleation is more likely, even in the presence of high pore pressures. Another possibility is that fluids inferred to be present during the postseismic phase were trapped below a sealed megathrust during the preseismic period and then released by the propagation of rupture. This could be consistent with the moderate-to-high preseismic locking degree in this area, which in turns implies that conditionally stable regions could become locked at some point before great earthquakes.

If this interpretation is correct, then the zone between 35° and 35.5°S, which coincides (Fig. 1) with a change in the density (higher in the north) and orientation (NE–SW in the north to NNE–SSW in the south) of bending-related fractures, could represent an area where fluids were already present at high pore pressure inside the megathrust before the earthquake. This for instance could favor interseismic creeping as suggested by low preseismic locking, predicting its possible behavior as a barrier for coseismic rupture propagation. Back projection of teleseismic waves (Kiser and Ishii, 2011; Wang and Mori, 2011; Koper et al., 2012) radiated from the megathrust during coseismic propagation of the Maule rupture toward the north suggest that the rupture front was decelerated by its pass through this region, perhaps as a consequence of rupturing a high pore pressure barrier. However, the front was finally able to surpass this barrier triggering the rapid slip on the large coseismic slip region northward of 35°S. This region seems to be located at the transition between the inferred high pore pressure barrier and a strongly locked preseismic patch. As this patch lies inside a region that we infer is dominated by the activity of fluids during the early (TT) postseismic phase, we again must conclude that high pore pressure, conditionally stable regions can become locked before an earthquake. The mechanism by which a high fluid megathrust can be eventually locked is unclear, but we suspect that is similar to what we propose for explaining the correlated decrease of afterslip and *b*-value during T2 for points in the northern half of the rupture area. This is either the consumption of pore fluids via crystallization of gouge minerals and/or the escape of fluids into the upper plate. Our results show (Fig. 8) that this fluid-consuming healing mechanism was still active in the north until the end of our time frame; a longer time analysis in future works could reveal whether this process finally ended up moving these northern points toward the lower-left corner of Fig. 7 (stick–slip, dry, healed regimen).

Whatever the case, our results suggest that frictional properties at the northern half of the ruptured segment are significantly different from those in the south. Here, the propagating coseismic front entered with relatively low speed liberating mostly low-frequency energy (Kiser and Ishii, 2011; Koper et al., 2012) by rupturing a high preseismic locking patch below the Arauco Peninsula. Our analysis suggests that this segment of the megathrust is mostly dry, as also pointed out by other authors (e.g. Cubas et al., 2013; Moreno et al., 2014), and dominated by a low fluid pressure, stick–slip behavior. This is consistent with the notable correlation between high preseismic locking, large coseismic slip and minor afterslip dominated by relatively large aftershocks (Lange et al., 2012; Rietbrock et al., 2012; Agurto et al., 2012) that we interpret as the consequence of the relaxation of the static stress change under low pore pressure. This patch nested the nucleation of the Mw 9.5 Valdivia 1960 giant earthquake and was largely ruptured by it, suggesting that dry megathrusts can heal and reconstitute high friction at the scale of decades. Our results show that this process was actually very rapid (months) after the Maule earthquake. Interestingly, the low *b*-value and minimum afterslip that characterize the Arauco Bay area (as exemplified by point H in Fig. 6) coincide with a region of reduced coseismic slip for relatively large preseismic locking. We speculate that this region could still be partially locked and able to generate a relatively large earthquake (Mw 7–7.5) in the near future, as also suggested by estimates of the slip deficit left after the Maule earthquake (Lorito et al., 2011; Moreno et al., 2012).

5.6. Strong versus weak asperities

Inside the seismogenic zone, i.e. where a rate-weakening frictional regime is expected, we document significant variations in the postseismic behavior along the segment ruptured by the Maule earthquake, which together with its pre- and coseismic behavior allows to propose a modification of the notion of seismic asperities with respect to the classical model of Lay and Kanamori (1981). The main features that characterize the southern segment (high preseismic locking, large coseismic slip, minimum afterslip, large aftershocks around the ruptured patch) coincide with what can be normally expected for a strong, high friction, stick–slip rate-weakening asperity. The evidence presented by us and by other authors reporting about the physical features along the Maule segment (Tassara, 2010; Moreno et al., 2014; Cubas et al., 2013; Hicks et al., 2012, 2014) suggest that such strong stick–slip asperities are only possible when the megathrust is significantly dry. Under these low fluid pressure conditions, the fault can heal quite rapidly, likely over the first years after a large earthquake as suggested by our results. This rapid healing below the Arauco region is also consistent with the fact that after the giant Valdivia earthquake 50 years before the Maule event, the megathrust here was able to accumulate sufficient elastic energy in order to liberate a slip of 5–10 m as for the 1960 event. On the other hand, strong and dry stick–slip asperities like the one below the Arauco region seems to radiate dominantly low-frequency energy (as reported by Kiser and Ishii, 2011; Koper et al., 2012), a feature which is probably due to the existence of a large and smooth region of the megathrust characterized by low pore pressures allowing the homogeneous propagation of the rupture front.

In contrast to the southerly strong asperity, the patch of large coseismic slip in the north presents a particular postseismic behavior that we interpreted as being caused by the pervasive presence of fluids into the megathrust and a conditionally stable frictional regimen owing to its high pore pressure. The occurrence of this large coseismic slip patch at the transition between a high preseismic locking at the northernmost extent of the ruptured segment and a less locked region toward the epicentral area implies that under such high fluid pressures, conditionally stable patches of the megathrust can become locked, building sufficient elastic strain and slip deficit in order to participate in the coseismic rupture. Regions like this can be considered asperities in the sense that they can be locked during the interseismic period and substantially contribute to the coseismic energy release, but we think that it is necessary to distinguish them from strong and dry asperities because they are fundamentally different in terms of their frictional behavior. Similar complex seismogenic behaviors that combine creeping, locking and coseismic slip on weak and conditionally stable patches has been documented in numerical simulations of the seismic cycle (Barbot et al., 2012; Noda and Lapusta, 2013; Kaneko et al., 2010). Wet regions of the megathrust like this can concentrate very large slip (actually, the northern slip patch of the Maule earthquake had 5–10 m of overshooting compared with the slip deficit built after the 1835 event; Moreno et al., 2012), radiating a larger proportion of high-frequency energy than dry and strong asperities (at least as suggested by the Maule earthquake by Kiser and Ishii (2011); Koper et al. (2012)). Thus, the conceptual recognition of such hazardous, weak, high fluid pressure and conditionally stable asperities is an important outcome of our study.

Acknowledgments

We thank the Chilean Fondecyt projects 1101034 and 1151175, and the International Scientific Collaboration Projects DAAD/Conicyt 2058-2010 and DFG/Conicyt PCCI130039. We use Generic Mapping Tools (GMT; Wessel and Smith, 1998) for most of the figures. We acknowledge comments and useful suggestions of the Editor, one anonymous reviewer and Rafael Bartolome.

Appendix A. Supplementary data

Supplementary data to this article can be found online at http://dx.doi.org/10.1016/j.tecto.2016.01.009.

References

Agurto, H., Rietbrock, A., Ryder, I., Miller, M., 2012. Seismic-afterslip characterization of the 2010 M W 8.8 Maule, Chile, earthquake based on moment tensor inversion. Geophys. Res. Lett. *39* (20). http://dx.doi.org/10.1029/2012GL053434 (n/a–n/a).

Aki, K., 1965. Maximum likelihood estimate of *b* in the formula log N = a − bM and its confidence limits. Bull. Earthquake Res. Inst. 43, 237–239.

Audet, P., Bostock, M.G., Christensen, N.I., Peacock, S.M., 2009. Seismic evidence for overpressured subducted oceanic crust and megathrust fault sealing. Nature 457, 76–78. http://dx.doi.org/10.1038/nature07650.

Bachmann, C.E., Wiemer, S., Goertz-Allmann, B.P., Woessner, J., 2012. Influence of pore-pressure on the event-size distribution of induced earthquakes. Geophys. Res. Lett. 39 (9). http://dx.doi.org/10.1029/2012GL051480 (n/a–n/a).

Barbot, S., Lapusta, N., Avouac, J.-P., 2012. Under the hood of the earthquake machine: toward predictive modeling of the seismic cycle. Science 336, 707–710. http://dx.doi.org/10.1126/science.1218796.

Bedford, J., Moreno, M., Baez, J.C., Lange, D., Tilmann, F., Rosenau, M., ... Vigny, C., 2013. A high-resolution, time-variable afterslip model for the 2010 Maule Mw = 8.8, Chile megathrust earthquake. Earth Planet. Sci. Lett. 383, 26–36. http://dx.doi.org/10.1016/j.epsl.2013.09.020.

Calahorrano, B.A., Sallarès, V., Collot, J.Y., Sage, F., Ranero, C.R., 2008. Nonlinear variations of the physical properties along the Southern Ecuador subduction channel: results from depth-migrated seismic data. Earth Planet. Sci. Lett. 267, 453–467. http://dx.doi.org/10.1016/j.epsl.2007.11.061.

Contreras-Reyes, E., Carrizo, D., 2011. Control of high oceanic features and subduction channel on earthquake ruptures along the Chile–Peru subduction zone. Phys. Earth Planet. Inter. 186, 49–58. http://dx.doi.org/10.1016/j.pepi.2011.03.002.

Contreras-Reyes, E., Osses, A., 2010. Lithospheric flexure modelling seaward of the Chile trench: implications for oceanic plate weakening in the Trench Outer Rise region. Geophys. J. Int. 182, 97–112. http://dx.doi.org/10.1111/j.1365-246X.2010.04629.x.

Contreras-Reyes, E., Grevemeyer, I., Flueh, E.R., Scherwath, M., Heesemann, M., 2007. Alteration of the subducting oceanic lithosphere at the southern central Chile trench-outer rise. Geochem. Geophys. Geosyst. 8. http://dx.doi.org/10.1029/2007GC001632.

Contreras-Reyes, E., Grevemeyer, I., Flueh, E.R., Reichert, C., 2008. Upper lithospheric structure of the subduction zone offshore of southern Arauco peninsula, Chile, at ~38°S. J. Geophys. Res. Solid Earth *113*. http://dx.doi.org/10.1029/2007JB005569.

Cubas, N., Avouac, J.P., Souloumiac, P., Leroy, Y., 2013. Megathrust friction determined from mechanical analysis of the forearc in the Maule earthquake area. Earth Planet. Sci. Lett. 381, 92–103. http://dx.doi.org/10.1016/j.epsl.2013.07.037.

Darwin, C., 1851. Geological Observations on Coral Reefs, Volcanic Islands, and on South America—Being the Voyage of the Beagle, Under the Command of Captain Fitzroy, R. N., during the Years 1832 to 1836. Smith Elder, London (279 pp.).

Delouis, B., Nocquet, J.M., Vallée, M., 2010. Slip distribution of the February 27, 2010 Mw = 8.8 Maule Earthquake, central Chile, from static and high-rate GPS, InSAR,

and broadband teleseismic data. Geophys. Res. Lett. 37. http://dx.doi.org/10.1029/2010GL043899.
Den Hartog, S.A.M., Spiers, C.J., 2013. Influence of subduction zone conditions and gouge composition on frictional slip stability of megathrust faults. Tectonophysics 600, 75–90. http://dx.doi.org/10.1016/j.tecto.2012.11.006.
Dieterich, J.H., 1979. Modeling of rock friction 1. Experimental results and constitutive equations. J. Geophys. Res. Solid Earth 84, 2161–2168. http://dx.doi.org/10.1029/JB084iB05p02161.
El-Isa, Z.H., Eaton, D.W., 2014. Spatiotemporal variations in the *b*-value of earthquake magnitude-frequency distributions: classification and causes. Tectonophysics 615-616, 1–11.
Faccenda, M., Gerya, T.V., Burlini, L., 2009. Deep slab hydration induced by bending-related variations in tectonic pressure. Nat. Geosci. http://dx.doi.org/10.1038/ngeo656.
Farías, M., Vargas, G., Tassara, A., Carretier, S., Baize, S., Melnick, D., Bataille, K., 2010. Land-level changes produced by the Mw 8.8 2010 Chilean earthquake. Science 329 (5994), 916 (Retrieved from (http://www.ncbi.nlm.nih.gov/pubmed/20671154).
Farías, M., Comte, D., Roecker, S., Carrizo, D., Pardo, M., 2011. Crustal extensional faulting triggered by the 2010 Chilean earthquake: the Pichilemu seismic sequence. Tectonics *30*. http://dx.doi.org/10.1029/2011TC002888.
Fritz, H.M., Petroff, C.M., Catalán, P.A., Cienfuegos, R., Winckler, P., Kalligeris, N., ... Synolakis, C.E., 2011. Field survey of the 27 February 2010 Chile tsunami. Pure Appl. Geophys. 168, 1989–2010. http://dx.doi.org/10.1007/s00024-011-0283-5.
Fukuda, J., Kato, A., Kato, N., Aoki, Y., 2013. Are the frictional properties of creeping faults persistent? Evidence from rapid afterslip following the 2011 Tohoku-Oki earthquake. Geophys. Res. Lett. 40, 3613–3617. http://dx.doi.org/10.1002/grl.50713.
Geissler, W.H., Matias, L., Stich, D., Carrilho, F., Jokat, W., Monna, S., ... Zitellini, N., 2010. Focal mechanisms for sub-crustal earthquakes in the Gulf of Cadiz from a dense OBS deployment. Geophys. Res. Lett. 37 (18).
Gischig, V.S., Wiemer, S., 2013. A stochastic model for induced seismicity based on non-linear pressure diffusion and irreversible permeability enhancement. Geophys. J. Int. 194, 1229–1249. http://dx.doi.org/10.1093/gji/ggt164.
Goebel, W.T.H., Schorlemmer, D., Becker, T.W., Dresen, G., Sammis, C.G., 2013. Acoustic emissions document stress changes over many seismic cycles in stick–slip experiments. Geophys. Res. Lett. 40 (10), 2049–2054. http://dx.doi.org/10.1002/grl.50507.
Goertz-Allmann, B., & Wiemer, S. (2012). Geomechanical modeling of induced seismicity source parameters and implications for seismic hazard assessment. Geophysics, 78(1). Retrieved from http://dx.doi.org/10.1190/geo2012-0102.1
Grevemeyer, I., Ranero, C.R., Flueh, E.R., Kläschen, D., Bialas, J., 2007. Passive and active seismological study of bending-related faulting and mantle serpentinization at the Middle America trench. Earth Planet. Sci. Lett. 258, 528–542. http://dx.doi.org/10.1016/j.epsl.2007.04.013.
Gutenberg, B., Richter, C.F., 1944. Frequency of earthquakes in California. Bull. Seismol. Soc. Am. 34 (4), 185–188.
Hamilton, R.M., 1967. Mean magnitude of an earthquake sequence. Bull. Seismol. Soc. Am. 57 (5), 1115–1116.
Hardebeck, J.L., 2012. Coseismic and postseismic stress rotations due to great subduction zone earthquakes. Geophys. Res. Lett. *39*. http://dx.doi.org/10.1029/2012GL053438.
Hicks, S.P., Rietbrock, A., Haberland, C.A., Ryder, I.M.A., Simons, M., Tassara, A., 2012. The 2010 Mw 8.8 Maule, Chile earthquake: nucleation and rupture propagation controlled by a subducted topographic high. Geophys. Res. Lett. 39. http://dx.doi.org/10.1029/2012GL053184.
Hicks, S.P., Rietbrock, A., Ryder, I.M., Lee, C.S., Miller, M., 2014. Anatomy of a megathrust: the 2010 M 8.8 Maule, Chile earthquake rupture zone imaged using seismic tomography. Earth Planet. Sci. Lett. 405, 142–155.
Hirono, T., Tanikawa, W., Honda, G., Kameda, J., Fukuda, J., Ishikawa, T., 2013. Importance of mechanochemical effects on fault slip behavior during earthquakes. Geophys. Res. Lett. 40 (12), 2988–2992. http://dx.doi.org/10.1002/grl.50609.
Hsu, Y.-J., Simons, M., Avouac, J.-P., Galetzka, J., Sieh, K., Chlieh, M., ... Bock, Y., 2006. Frictional afterslip following the 2005 Nias–Simeulue earthquake, Sumatra. Science (New York, N.Y.) 312, 1921–1926. http://dx.doi.org/10.1126/science.1126960.
Hu, Y., Wang, K., 2012. Spherical-Earth finite element model of short-term postseismic deformation following the 2004 Sumatra earthquake. J. Geophys. Res. http://dx.doi.org/10.1029/2012JB009153.
Johnson, K.M., Fukuda, J., Segall, P., 2012. Challenging the rate-state asperity model: afterslip following the 2011 M 9 Tohoku-Oki, Japan, earthquake. Geophys. Res. Lett. *39*. http://dx.doi.org/10.1029/2012GL052901.
Kaneko, Y., Avouac, J.-P., Lapusta, N., 2010. Towards inferring earthquake patterns from geodetic observations of interseismic coupling. Nat. Geosci. 3 (5), 363–369. http://dx.doi.org/10.1038/ngeo843.
Kendrick, E., Bevis, M., Smalley, R., Brooks, B., Vargas, R.B., Lauria, E., Fortes, L.P.S., 2003. The Nazca–South America Euler vector and its rate of change. J. S. Am. Earth Sci. 16 (2), 125–131.
Kiser, E., Ishii, M., 2011. The 2010 Mw 8.8 Chile earthquake: triggering on multiple segments and frequency-dependent rupture behavior. Geophys. Res. Lett. 38 (April), 6–11. http://dx.doi.org/10.1029/2011GL047140.
Koerner, A., Koerner, A., Kissling, E., Kissling, E., Miller, S.A., Miller, S.A., 2004. A model of deep crustal fluid flow following the M-w = 8.0 Antofagasta, Chile, earthquake. J. Geophys. Res. *109*. http://dx.doi.org/10.1029/2003JB002816.
Koper, K.D., Hutko, A.R., Lay, T., Sufri, O., 2012. Imaging short-period seismic radiation from the 27 February 2010 Chile (MW 8.8) earthquake by back-projection of P, PP, and PKIKP waves. J. Geophys. Res. Solid Earth. http://dx.doi.org/10.1029/2011JB008576.
Kositsky, A.P., Avouac, J.P., 2010. Inverting geodetic time series with a principal component analysis-based inversion method. J. Geophys. Res. Solid Earth *115*. http://dx.doi.org/10.1029/2009JB006535.
Lange, D., Tilmann, F., Barrientos, S.E., Contreras-Reyes, E., Methe, P., Moreno, M., ... Beck, S., 2012. Aftershock seismicity of the 27 February 2010 Mw 8.8 Maule earthquake rupture zone. Earth Planet. Sci. Lett. 317-318, 413–425. http://dx.doi.org/10.1016/j.epsl.2011.11.034.
Lange, D., Bedford, J.R., Moreno, M., Tilmann, F., Baez, J.C., Bevis, M., Krüger, F., 2014. Comparison of postseismic afterslip models with aftershock seismicity for three subduction-zone earthquakes: Nias 2005, Maule 2010 and Tohoku 2011. Geophys. J. Int. 199 (2), 784–799.
Lay, T., Kanamori, H., 1981. An asperity model of large earthquake sequences. Earthq. Prediction 579–592.
Lay, T., Ammon, C.J., Kanamori, H., Koper, K.D., Sufri, O., Hutko, A.R., 2010. Teleseismic inversion for rupture process of the 27 February 2010 Chile (Mw 8.8) earthquake. Geophys. Res. Lett. *37* (13). http://dx.doi.org/10.1029/2010GL043379 (n/a–n/a).
Legrand, D., Tassara, A., Morales, D., 2012. Megathrust asperities and clusters of slab dehydration identified by spatiotemporal characterization of seismicity below the Andean margin. Geophys. J. Int. 191, 923–931. http://dx.doi.org/10.1111/j.1365-246X.2012.05682.x.
Lieser, K., Grevemeyer, I., Lange, D., Flueh, E., Tilmann, F., Contreras-Reyes, E., 2014. Splay fault activity revealed by aftershocks of the 2010 Mw 8.8 Maule earthquake, central Chile. Geology 42, 823–826. http://dx.doi.org/10.1130/G35848.1.
Lin, Y.N.N., Sladen, A., Ortega-Culaciati, F., Simons, M., Avouac, J.P., Fielding, E.J., ... Socquet, A., 2013. Coseismic and postseismic slip associated with the 2010 Maule Earthquake, Chile: characterizing the Arauco Peninsula barrier effect. J. Geophys. Res. Solid Earth 118 (6), 3142–3159. http://dx.doi.org/10.1002/jgrb.50207.
Lorito, S., Romano, F., Atzori, S., Tong, X., Avallone, A., McCloskey, J., ... Piatanesi, A., 2011. Limited overlap between the seismic gap and coseismic slip of the great 2010 Chile earthquake. Nat. Geosci. http://dx.doi.org/10.1038/ngeo1073.
Maksymowicz, A., Trehu, A., Contreras-Reyes, E., Ruiz, S., 2015. Density-depth model of the continental wedge at the maximum slip segment of the Maule Mw8.8 megathrust earthquake. Earth Planet. Sci. Lett. 409, 265–277. http://dx.doi.org/10.1016/j.epsl.2014.11.005.
Marone, C., 1998. Laboratory-derived friction laws and their application to seismic faulting. Annu. Rev. Earth Planet. Sci. http://dx.doi.org/10.1146/annurev.earth.26.1.643.
Marzocchi, W., Sandri, L., 2003. A review and new insights on the estimation of the *b*-value and its uncertainty. Ann. Geophys. 46, 1271–1282.
Melnick, D., Cisternas, M., Moreno, M., Norambuena, R., 2012a. Estimating coseismic coastal uplift with an intertidal mussel: calibration for the 2010 Maule Chile earthquake (Mw = 8.8). Quat. Sci. Rev. 42, 29–42. http://dx.doi.org/10.1016/j.quascirev.2012.03.012.
Melnick, D., Moreno, M., Cisternas, M., Tassara, A., 2012b. Darwin' seismic gap closed by the 2010 Maule earthquake. Andean Geol. http://dx.doi.org/10.5027/andgeoV39n3-a11.
Métois, M., Socquet, A., Vigny, C., 2012. Interseismic coupling, segmentation and mechanical behavior of the central Chile subduction zone. J. Geophys. Res. Solid Earth *117*. http://dx.doi.org/10.1029/2011JB008736.
Moreno, M.S., Bolte, J., Klotz, J., Melnick, D., 2009. Impact of megathrust geometry on inversion of coseismic slip from geodetic data: application to the 1960 Chile earthquake. Geophys. Res. Lett. *36*. http://dx.doi.org/10.1029/2009GL039276.
Moreno, M., Rosenau, M., Oncken, O., 2010. 2010 Maule earthquake slip correlates with pre-seismic locking of Andean subduction zone. Nature 467, 198–202. http://dx.doi.org/10.1038/nature09349.
Moreno, M., Melnick, D., Rosenau, M., Baez, J., Klotz, J., Oncken, O., ... Hase, H., 2012. Toward understanding tectonic control on the Mw 8.8 2010 Maule Chile earthquake. Earth Planet. Sci. Lett. 321-322, 152–165. http://dx.doi.org/10.1016/j.epsl.2012.01.006.
Moreno, M., Haberland, C., Oncken, O., Rietbrock, A., Angiboust, S., Heidbach, O., 2014. Locking of the Chile subduction zone controlled by fluid pressure before the 2010 earthquake. Nat. Geosci. 7, 292–296. http://dx.doi.org/10.1038/NGEO2102.
Moscoso, E.I., Contreras-Reyes, E., 2012. Outer rise seismicity related to the Maule, Chile 2010 mega-thrust earthquake and hydration of the incoming oceanic lithosphere. Andean Geol. http://dx.doi.org/10.5027/andgeoV39n3-a12.
Moscoso, E., Grevemeyer, I., Contreras-Reyes, E., Flueh, E.R., Dzierma, Y., Rabbel, W., Thorwart, M., 2011. Revealing the deep structure and rupture plane of the 2010 Maule, Chile earthquake (Mw = 8.8) using wide angle seismic data. Earth Planet. Sci. Lett. 307, 147–155. http://dx.doi.org/10.1016/j.epsl.2011.04.025.
Nakatani, M., Scholz, C.H., 2006. Intrinsic and apparent short-time limits for fault healing: theory, observations, and implications for velocity-dependent friction. J. Geophys. Res. Solid Earth 111. http://dx.doi.org/10.1029/2005JB004096.
Noda, H., Lapusta, N., 2013. Stable creeping fault segments can become destructive as a result of dynamic weakening. Nature 493, 518–521. http://dx.doi.org/10.1038/nature11703.
Oleskevich, D.A., Hyndman, R.D., Wang, K., 1999. The updip and downdip limits to great subduction earthquakes: thermal and structural models of Cascadia, south Alaska, SW Japan, and Chile. J. Geophys. Res. http://dx.doi.org/10.1029/1999JB900060.
Omori, F., 1894. On after-shocks of earthquakes. J. Coll. Sci. Imp. Univ. Tokyo 7, 111–200.
Ozawa, S., Nishimura, T., Munekane, H., Suito, H., Kobayashi, T., Tobita, M., Imakiire, T., 2012. Preceding, coseismic, and postseismic slips of the 2011 Tohoku earthquake, Japan. J. Geophys. Res. Solid Earth *117*. http://dx.doi.org/10.1029/2011JB009120.
Perfettini, H., Avouac, J.P., 2004. Postseismic relaxation driven by brittle creep: a possible mechanism to reconcile geodetic measurements and the decay rate of aftershocks, application to the Chi-Chi earthquake, Taiwan. J. Geophys. Res. Solid Earth (1978–2012) 109 (B2).
Perfettini, H., Avouac, J.-P., Tavera, H., Kositsky, A., Nocquet, J.-M., Bondoux, F., ... Soler, P., 2010. Seismic and aseismic slip on the central Peru megathrust. Nature 465, 78–81. http://dx.doi.org/10.1038/nature09062.
Ranero, C.R., Morgan, J.P., McIntosh, K., Reichert, C., 2003. Bending-related faulting and mantle serpentinization at the Middle America trench. Nature 425, 367–373. http://dx.doi.org/10.1038/nature01961.

Rietbrock, A., Ryder, I., Hayes, G., Haberland, C., Comte, D., Roecker, S., Lyon-Caen, H., 2012. Aftershock seismicity of the 2010 Maule Mw = 8.8, Chile, earthquake: correlation between co-seismic slip models and aftershock distribution? Geophys. Res. Lett. *39*. http://dx.doi.org/10.1029/2012GL051308.

Ruegg, J.C., Rudloff, A., Vigny, C., Madariaga, R., de Chabalier, J.B., Campos, J., ... Dimitrov, D., 2009. Interseismic strain accumulation measured by GPS in the seismic gap between Constitución and Concepción in Chile. Phys. Earth Planet. Inter. 175 (1–2), 78–85. http://dx.doi.org/10.1016/j.pepi.2008.02.015.

Ruina, A., 1983. Slip instability and state variable friction laws. J. Geophys. Res. Solid Earth (1978–2012) 88 (B12), 10359–10370.

Ryder, I., Rietbrock, A., Kelson, K., Bürgmann, R., Floyd, M., Socquet, A., ... Carrizo, D., 2012. Large extensional aftershocks in the continental forearc triggered by the 2010 Maule earthquake, Chile. Geophys. J. Int. 188, 879–890. http://dx.doi.org/10.1111/j.1365-246X.2011.05321.x.

Scholz, C.H., 1968. Experimental study of the fracturing process in brittle rock. J. Geophys. Res. 73 (4), 1447–1454.

Scholz, C.H., 1998. Earthquakes and friction laws. Nature 391, 37–42. http://dx.doi.org/10.1038/34097.

Scholz, C.H., 2015. On the stress dependence of the earthquake *b*-value. Geophys. Res. Lett. 10964. http://dx.doi.org/10.1002/2014GL062863 (n/a–n/a).

Schorlemmer, D., Wiemer, S., Wyss, M., 2005. Variations in earthquake-size distribution across different stress regimes. Nature 437, 539–542. http://dx.doi.org/10.1038/nature04094.

Sibson, R.H., 2013. Stress switching in subduction forearcs: implications for overpressure containment and strength cycling on megathrusts. Tectonophysics 600, 142–152. http://dx.doi.org/10.1016/j.tecto.2013.02.035.

Sparkes, R., Tilmann, F., Hovius, N., Hillier, J., 2010. Subducted seafloor relief stops rupture in South American great earthquakes: implications for rupture behaviour in the 2010 Maule, Chile earthquake. Earth Planet. Sci. Lett. 298 (1), 89–94.

Sun, T., Wang, K., Iinuma, T., Hino, R., He, J., Fujimoto, H., ... Hu, Y., 2014. Prevalence of viscoelastic relaxation after the 2011 Tohoku-Oki earthquake. Nature 514 (7520), 84–87.

Tassara, A., 2010. Control of forearc density structure on megathrust shear strength along the Chilean subduction zone. Tectonophysics 495, 34–47. http://dx.doi.org/10.1016/j.tecto.2010.06.004.

Tilmann, F., Grevemeyer, I., Flueh, E.R., Dahm, T., Gossler, J., 2008. Seismicity in the outer rise offshore southern Chile: indication of fluid effects in the crust and mantle. Earth Planet. Sci. Lett. 269, 41–55. http://dx.doi.org/10.1016/j.epsl.2008.01.044.

Tong, X., Sandwell, D., Luttrell, K., Brooks, B., Bevis, M., Shimada, M., ... Caccamise, D.J., 2010. The 2010 Maule, Chile earthquake: downdip rupture limit revealed by space geodesy. Geophys. Res. Lett. *37*. http://dx.doi.org/10.1029/2010GL045805.

Tormann, T., Enescu, B., Woessner, J., Wiemer, S., 2015. Randomness of megathrust earthquakes implied by rapid stress recovery after the Japan earthquake. Nat. Geosci. 8 (2), 152–158.

Utsu, T., Ogata, Y., Matsu'ura, R.S., 1995. The centenary of the Omori formula for a decay law of aftershock activity. J. Phys. Earth 43 (1), 1–33.

Van Stiphout, T., Kissling, E., Wiemer, S., Ruppert, N., 2009. Magmatic processes in the Alaska subduction zone by combined 3-D *b* value imaging and targeted seismic tomography. J. Geophys. Res. Solid Earth (1978–2012) 114 (B11).

Vargas, G., Farías, M., Carretier, S., Tassara, A., Baize, S., Melnick, D., 2011. Coastal uplift and tsunami effects associated to the 2010 Mw 8. 8 Maule earthquake in Central Chile. Andean Geol. 38, 219–238.

Vigny, C., Socquet, A., Peyrat, S., Ruegg, J.-C., Métois, M., Madariaga, R., ... Kendrick, E., 2011. The 2010 Mw 8.8 Maule megathrust earthquake of Central Chile, monitored by GPS. Science (New York, N.Y.) 332, 1417–1421. http://dx.doi.org/10.1126/science.1204132.

Wang, D., Mori, J., 2011. Frequency-dependent energy radiation and fault coupling for the 2010 Mw 8.8 Maule, Chile, and 2011 Mw 9.0 Tohoku, Japan, earthquakes. Geophys. Res. Lett. 38 (22).

Wessel, P., Smith, W.H.F., 1998. New, improved version of generic mapping tools released. Eos Trans. AGU 79 (47). http://dx.doi.org/10.1029/98EO00426 579–579.

Wiemer, S., Katsumata, K., 1999. Spatial variability of seismicity parameters in aftershock zones. J. Geophys. Res. Solid Earth (1978–2012) 104 (B6), 13135–13151.

Wiemer, S., Wyss, M., 2002. Mapping spatial variability of the frequency–magnitude distribution of earthquakes. Adv. Geophys. 45, 259-V.

Yasuhara, H., Marone, C., Elsworth, D., 2005. Fault zone restrengthening and frictional healing: the role of pressure solution. J. Geophys. Res. Solid Earth (1978–2012) 110 (B6).